Ore Geology Reviews 72 (2016) 191–212

Contents lists available at ScienceDirect

Ore Geology Reviews

journal homepage: www.elsevier.com/locate/oregeorev

Extreme enrichment of rare earth elements in hard clay rocks and its potential as a resource

Zhengwei Zhang [a,*], Guodong Zheng [b,*], Yoshio Takahashi [b,c], Chengquan Wu [a,d], Chaofei Zheng [a,d], Junhua Yao [a,d], Chaoyi Xiao [a,d]

[a] State Key Laboratory of Ore Deposit Geochemistry, Institute of Geochemistry, Chinese Academy of Sciences, 46 Guanshui Road, Guiyang 550002, China
[b] Key Laboratory of Petroleum Resources, Gansu Province/Key Laboratory of Petroleum Resources Research, Institute of Geology and Geophysics, Chinese Academy of Sciences, 382 West Donggang Road, Lanzhou 730000, China
[c] Department of Earth and Planetary Science, Graduate School of Science, The University of Tokyo, Hongo 7-3-1, Bunkyo-ku, Tokyo 113-0033, Japan
[d] University of Chinese Academy of Sciences, Beijing 100049, China

ARTICLE INFO

Article history:
Received 14 December 2014
Received in revised form 21 July 2015
Accepted 22 July 2015
Available online 26 July 2015

Keywords:
Kaolinitic clay rocks
Carbonaceous shale
Rare earth element
Western Guizhou

ABSTRACT

The Xuanwei Formation is widely distributed in western Guizhou Province, NW China, the lower section of which is primarily composed of gray-white kaolinitic claystone interbedded with thin layers of grayish black carbonaceous mudstone that are extremely enriched with rare earth elements. In order to determine the distribution patterns and existing status of ore-forming elements in these rocks, careful field investigations were performed along a selected geological profile and rock samples were collected and studied in terms of mineralogical and geochemical characteristics. The results show that: 1) REEs are primarily enriched in the grayish white kaolinitic clay sediments and grayish black carbonaceous mudstone. Mineralogical analyses revealed kaolinite as the major mineral in rocks along with smaller amounts of smectite, illite, boehmite, hornblende, pyrophyllite, calcite, dolomite and/or iron-bearing minerals, as well as a certain proportion of feldspar, quartz crystal debris and non-crystal debris. 2) $\sum$REE contents are 89.0 to 9965 ppm with an average of 1312 ppm. The thickness of the host rock with $\sum$REE higher than 1300 ppm is more than 4 m, which is referred to as the "REE-enriched layer". 3) The REE contents of bulk rocks exhibit a negative correlation with kaolinite, positive correlations with boehmite, hornblende and iron-bearing minerals, and weak positive correlations with smectite, illite and pyrophyllite, indicating that the REE might exist in an ion adsorption state in the space between the layers of clay minerals. 4) Compared with the underlying Emeishan Basalts, the REE patterns of samples are quite similar but are enriched in both LREE and HREE. The degree of enrichment of HREE is relatively high. Based on these results, a model is suggested where the REE-enriched layers originated from the Emeishan Basalts and were controlled by the transportation and deposition of detritus from a paleo-weathering crust. The hard clay rocks have a significant resource potential, as the contents of REE, Ga, Nb and Zr are considerably higher than those in the weathering crust type of REE deposit.

1. Introduction

The deposits of rare earth elements (REE) discovered throughout China to date can be generally classified into several types, including the Bayan Obo type (Qiu et al., 1981; Liu, 1985; Cao et al., 1994; Fan et al., 2002), the REE ores related to felsic-alkaline magma and/or hydrothermal fluids (Zhang, 1989); the supergene type (Wu et al., 1990; Zhang, 1994; Li et al., 2005; Bao and Zhao, 2008); the deep sea soft mud type (Kato et al., 2011); and REE ores associated with phosphorite and bauxite (Liu et al., 2006; Zhang et al., 2007; Wang et al., 2010). Relatively speaking, most research mainly focused on the significance of metamorphosed carbonatites, igneous rocks and residual clays to the ore formation of REE deposits (Kynicky et al., 2012), and the REE deposits related to sedimentary rocks are rarely reported (Zhang, 1989). However, some recent studies (e.g., Huang, 1997; Liu et al., 2010) revealed a series in the lower part of the latter Permian lacustrine to intertidal interbedded clastic rocks in western Guizhou Province, China, that is extremely enriched with REEs and rare metals. The latter Permian sequences in this area are referred to as the Xuanwei Formation, and the lower part of this sequence is mainly composed of kaolinitic clay rocks that are interbedded with carbonaceous clay stone and pelitic shale as the host rocks. These sequences are distributed regionally overlying the Emeishan Basalt Formation. There is a disconformity between these two formations, along which there is a typical paleo-weathered crust and a clay rock series, so that these REEs have been considered as a paleo-weathered (supergene) type of REE deposit (Yang et al.,

* Corresponding authors.
E-mail addresses: Zhangzhengw@hotmail.com (Z. Zhang), gdzhbj@mail.iggcas.ac.cn (G. Zheng).

http://dx.doi.org/10.1016/j.oregeorev.2015.07.018
0169-1368/

2008). However, considering their sedimentary characteristics, the host rocks should belong to typical lacustrine to intertidal interbedded clastic facies, or to general paleo-weathering crust deposits. Thus, these deposits might be considered as a sedimentary type of kaolinitic clay rock with REE (Zhou et al., 2013). According to our study, the main reason why these rocks, which are extremely enriched with rare earth elements, have not been industrially developed and utilized is probably due to a lack of information about the speciation or chemical status of REE in the rocks. Although the rocks contain very high contents of ore forming elements, most of them are richer in REE, Ga, Nb, and Zr than some commercial REE deposits in China (China Mineral Resources Reserves Committee, 1987; Kynicky et al., 2012; Migaszewski and Gałuszka, 2015; Emsbo et al., 2015; Chakhmouradian et al., 2015; Simandl, 2014; de Boer and Lammertsma, 2013). The ore forming elements rarely occur as individual minerals and are also distributed separately in the clay rocks. Their distribution patterns and occurrence status are not clear, which lead to some uncertainties in industrial development of the deposits and commercial extraction of the metals. Because of their unusual occurrence, the thickness and elemental contents of these rocks are still unknown, and it is difficult to know the occurrence/dimension of the "ore". At present, the REE-enriched rocks may not be designated as meaningful deposits, but they might be called "minerals" that could be exploited through a new mineral processing technique. In addition, these sequences are stratigraphic horizons with thicknesses that are very constant regionally; thus, they have potential to become sedimentary controlled REE deposits. Therefore, the spatial distribution of the ore forming elements is investigated through field measurement and analysis of some selected geological profiles in this paper. The occurrence status of ore forming elements in the rocks is identified based on mineralogical, petrological and geochemical studies, and their enrichment mechanism will subsequently be discussed based on previous research.

2. Geological background

The study area (Fig. 1), located in the southwestern margin of the Yangtze Craton, is part of the Upper Yangtze Craton Basin with mainly passive continental margin sedimentary sequences deposited since the Sinian period. There are outcrops of the Carboniferous, Permian, Triassic and Jurassic rocks, such as the Permian Maokou, Emeishan and Xuanwei Formations, and the Triassic Feixianguan Formation. The local volcanic rocks are mainly composed of Permian continental flood tholeiitic basalts. The axes of the regional folds are all distributed in the northeast direction, indicating the similar regional tectonic stress. The central parts of the folds are often composed of Jurassic sequences, probably indicating that the folding occurred between the Jurassic and Cretaceous periods. Thus, the Yanshanian tectonic event was very important for the development of the regional anticlines and synclines.

The Upper Permian Xuanwei Formation, enriched with REEs, Ga, Nb, Zr and other ore forming elements, is mainly composed of grayish

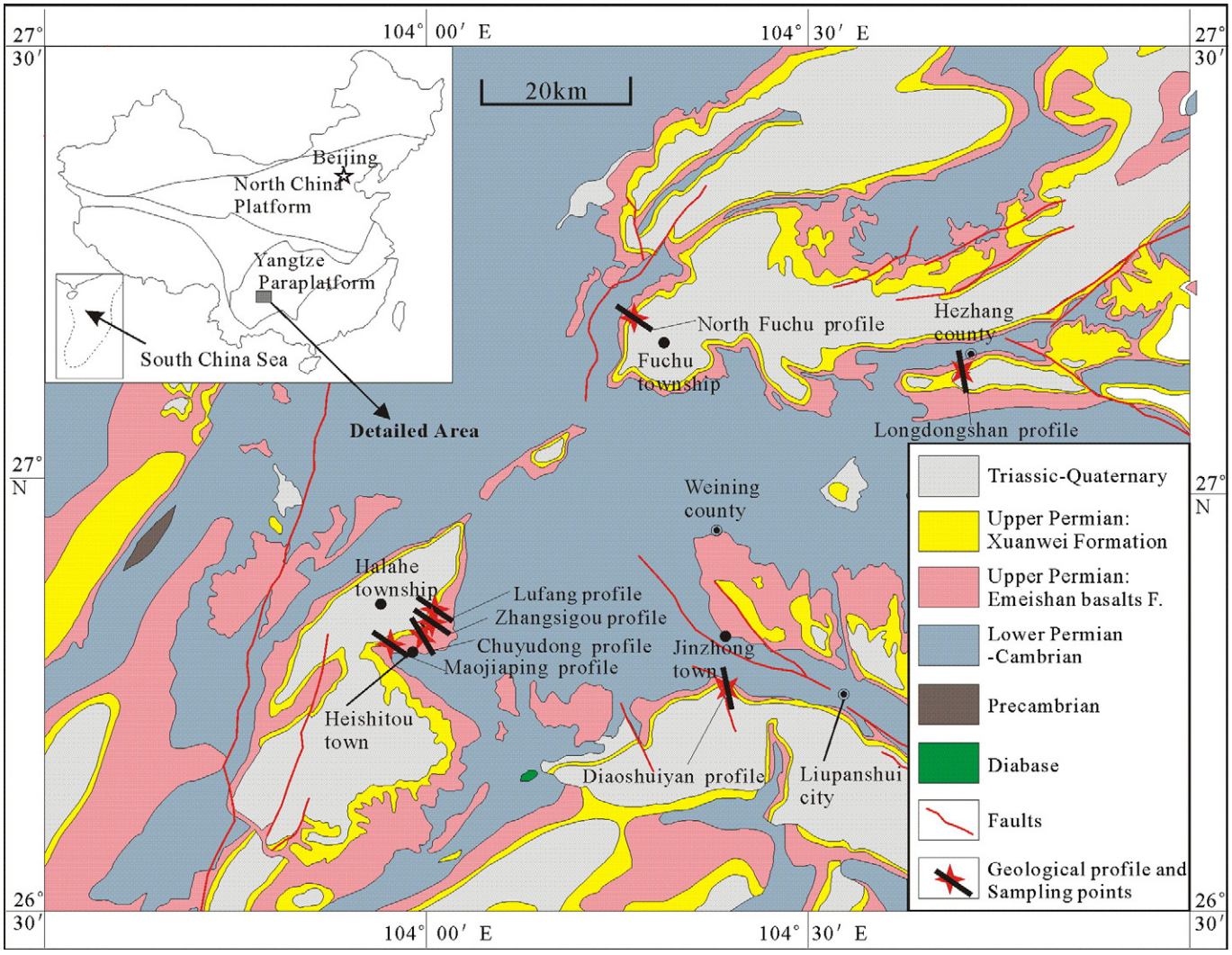

Fig. 1. Geological map of the study area and the locations of the geological sections.

yellow, light gray to dark gray mudstones (clay rocks), shales, interbedded with yellowish green, light-brown medium-thick layers of sandstones, siltstones, carbonaceous shales and various coal seams. In some areas, there are thin layers of purplish red tuff, tuffaceous shales, grayish green tuffaceous sandstones, and lenticular and sandy limestones (Fig. 2). There are numerous basalt fragments in the sandstone, the content of which may reach 10–35% in a few samples. The shale layers are interbedded with lenticular, quasi laminate, and nodular siderite and ripidolite. There is a widely distributed thin layer (0.2–0.3 m) at the bottom of the Xuanwei Formation, containing nodular hematite and siderite with an iron ore deposit consisting of iron-bearing chlorite clay rock. In some other areas, the lower sequence is interbedded with tuffaceous sandstone (hematite, siderite) and tuffaceous shale, and the upper part is interbedded with limestone and sandy limestone. In the early period of deposition of the Xuanwei Formation, the sediments were probably sourced from the continental Emeishan Basalt Formation.

The Xuanwei Formation was geologically investigated and first reported by Xie (1963), and the primary unit investigated was the Xuanwei coal series with latter Permian terrestrial sediments of coal-bearing sandy shale in the Eastern Yunnan Province and Western Guizhou Province, southwest China. Along with the following intensive investigations and studies, this sedimentary sequence had been divided into two parts. The upper part is mainly continental coal-bearing sandy shale (Chen et al., 2003; Mei et al., 2007), whereas the lower part consists of coal-bearing clastic rocks covered by ancient weathered crusts on the surface with different thicknesses that unconformably covered the Emeishan Basalts (Huang, 1997; Wang et al, 2006). On the geological sections, weathered basaltic and tuffaceous rocks were found, and also some typical mineralization of iron and copper was observed, which was considered as being related to strong weathering after the eruption of the Emeishan Basalts (Geological Team 108, Guizhou Bureau of Geology and Mineral Resources, 1973; Yang et al., 2008; Yang et al., 2011).

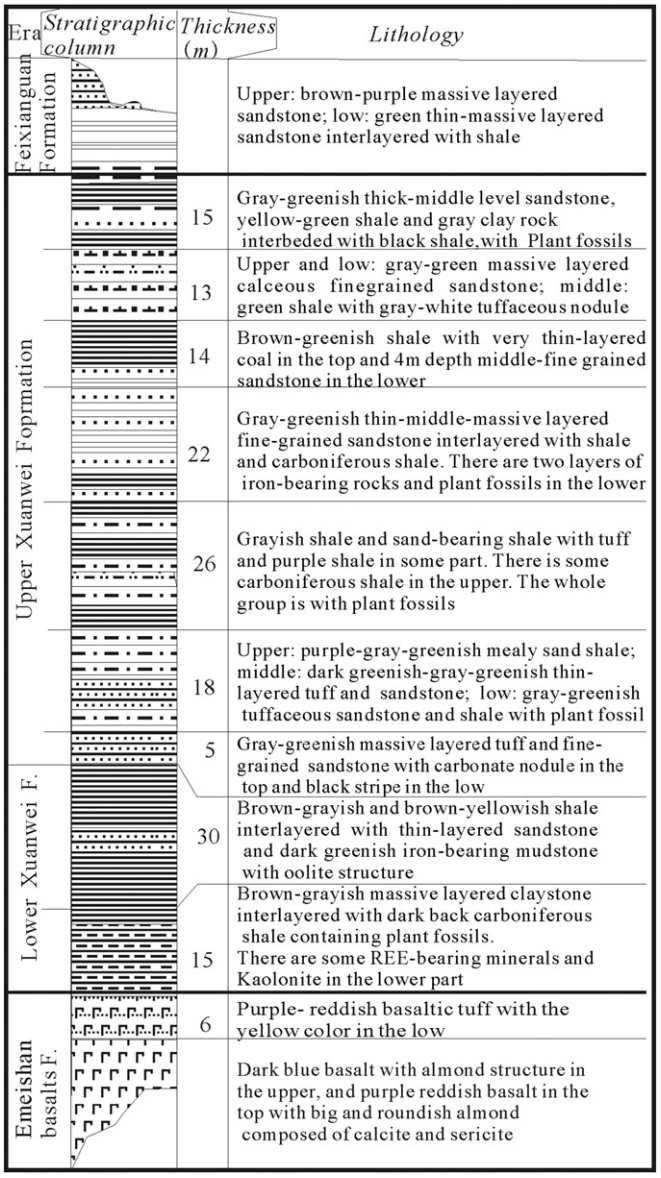

Fig. 2. Stratigraphic column of the Xunwei Formation.
After Geology Team 108, Guizhou Bureau of Geology and Mineral Resources (1973).

The lower part of the Xuanwei Formation exhibits strong hydrothermal alteration with some mineralization. For example, the Laoyingyan rocks are highly enriched in copper (Zhu et al., 2003), and there is mineralization of siderite and chalcopyrite in the layers near the village of Zhangsigou in Weining County (Zhang et al., 2003); additionally, chalcopyrite and native copper are related to carbonaceous and silicified wood in the Heishanpo section in Xiweining County (Zhang et al., 2004). Other than the REE-bearing minerals and siderite, hematite, and chalcopyrite, there is also some enrichment of Ga, Nb, Zr, etc. (Zhang et al., 2010a,b). The Rb–Sr dating of the carbonaceous shale in the lower part of the Xuanwei Formation yielded an age of 255 Ma (Xu et al., 2006). This layer of carbonaceous shale disconformably covered the tuff layer at the top part of the basalt formation and is stably and widely distributed. Thus, the emplacement of the Emeishan Basalts would have terminated before 255 Ma, being approximately 4 Ma earlier than 251 Ma, which was widely considered as the boundary between the Permian and Triassic periods (Yin, 1994). This time difference was mostly fit for the deposition period of the Xuanwei Formation because the Emeishan Basalts were denuded and then subsided to receive approximately 100 m of sediments. The age of 255 Ma for the carbonaceous shale is consistent with the sedimentary sequences. This age is the lower limit for the deposition of the Xuanwei Formation, and also the upper limit for the eruption of the Emeishan Basalts because the Xuanwei Formation covered the Emeishan Basalt Formation directly with a parallel disconformity; the latter was dated exactly as 256 Ma (Zhou et al., 2002), probably indicating that a relatively stable sedimentary basin developed after the Emeishan Basalt eruption ended.

The Emeishan Basalt Formation is widely distributed in the study area and is dominated by dense black basalt, dark-green massive and amygdaloidal basalts, and albitized basalt. These rocks are also interbedded with yellow-brown basaltic sediments, tuff, tuffaceous clay rocks, argillaceous sandy conglomerate, and so on (Xu et al., 2001; Zhou et al., 2002; Hu et al., 2005).

To investigate the regional correlation between the Xuanwei Formation and the underlying Emeishan Basalt Formation, a field geological transect was carried out in the vicinity of the village of Chuyudong, and rock samples were collected from the Emeishan Basalt Formation along the section (Fig. 3). This village, belonging to the town of

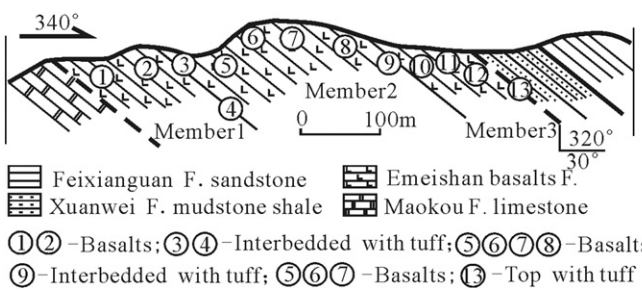

Fig. 3. Longitudinal profile of the geological transect in Chuyudong Village. The numbers of samples (1–13) correspond to CSD-1 to CSD-13.

Table 1
Major element (in %) and trace element (in ppm) concentrations of the Emeishan Basalts in Chuyudong.

Sample	CSD-1	CSD-2	CSD-3	CSD-4	CSD-5	CSD-6	CSD-7	CSD-8	CSD-9	CSD-10	CSD-11	CSD-12	CSD-13
SiO_2	48.13	49.3	67.85	69.83	47.52	49.1	48.22	45	32.02	47.25	47.56	45.51	38.53
Al_2O_3	13.65	13.32	7.23	4.31	13.04	12.92	13.69	14.22	22.05	13.49	13.03	13.27	18.27
Fe_2O_{3T}	13.41	13.48	7.68	3.09	14.06	14.81	13.87	14.61	22.86	14.84	16.11	15.15	18.66
CaO	8.96	8.43	2.58	1.01	7.97	8.55	4.88	9.51	0.88	9.6	5.71	7.54	0.83
MgO	4.79	4.32	2.4	0.55	4.36	4.17	4.16	5.13	0.82	4.79	4.51	5.07	2.24
Na_2O	2.09	2.4	1.18	0.02	2.01	2.09	4.04	2.72	0.08	2.82	5.32	3.39	0.04
K_2O	1.21	0.81	0.27	2.51	1.55	1.31	1.27	0.21	1.31	0.95	0.13	0.56	5.23
TiO_2	4.16	3.83	1.83	0.83	3.85	4.46	4.71	4.52	6.47	3.29	3.14	3.76	5.13
MnO	0.19	0.17	0.07	0.01	0.17	0.2	0.2	0.29	0.16	0.2	0.25	0.23	0.15
P_2O_5	0.43	0.372	0.192	0.046	0.417	0.498	0.486	0.451	0.191	0.332	0.321	0.418	0.453
LOI	2.54	2.23	7.29	16.8	3.55	1.4	3.82	3.11	11.9	2.07	2.43	3.18	9.03
Ba	435	369	72.1	158.5	379	451	341	179.5	319	241	53.2	181.5	547
Co	32.6	35.2	17.5	8.3	37.1	35.4	37.7	37.3	25.5	37.3	37.1	40.3	44.4
Cr	90	50	40	10	40	30	30	30	30	100	130	30	40
Ga	24.4	24.3	19.1	6.4	24.5	24.7	27.2	24.7	33.2	23.2	23.9	23.3	34.3
Hf	9	7.8	3.8	1.9	8.4	8.7	10.2	7.9	13.8	5.7	6.5	7	9.1
Nb	40	35	16.7	7.9	39	45.8	50.7	41.1	47.6	25.5	24.7	37.1	39.6
Rb	22.3	51.3	12.7	56.9	51.4	30.5	28	1.9	48.7	22.1	2.5	9.3	221
Sr	560	704	303	62.5	576	550	283	572	150	328	138	347	83.6
Ta	2.5	1.9	0.9	0.5	2.3	2.5	3	2.5	2.3	1.5	1.2	2.3	1.9
Th	6.84	7.36	3.28	2.08	6.65	7.55	8.04	6.29	11.35	4.03	4.08	5.54	8.06
U	1.52	1.77	0.78	3.73	1.55	1.78	1.7	1.47	3.19	1.02	1.07	1.24	1.52
V	397	365	169	370	411	396	442	412	354	367	367	407	478
Zr	348	328	154	76	330	372	405	315	534	216	279	270	370
Cu	221	157	170	122	206	213	206	384	93	227	208	153	15
La	45.2	41.9	20.6	46.5	41.7	49.5	47.9	42.7	136.5	26.3	28.7	36	96.5
Ce	100	94.5	44.3	35	93.1	110.5	114	96.8	229	58.1	62.4	84.2	102.5
Pr	13.25	12.45	5.95	7.92	12.3	14.65	15.65	12.85	28.9	7.86	8.24	11.15	27
Nd	51.6	49.7	23.7	32.5	49.7	57.7	62.1	50.8	95.4	31.4	33.5	42.8	96.1
Sm	11	10.4	5.26	5.51	10.85	12.25	13.5	10.9	14.35	7.65	8.16	9.31	19.85
Eu	3.3	2.86	1.38	1.4	3.14	3.63	3.84	3.24	4.22	2.4	2.57	2.76	5.45
Gd	9.54	8.11	4.41	5.3	9.06	10.3	10.9	8.98	10.1	7.18	7.62	8.01	15.45
Tb	1.33	1.2	0.67	0.66	1.32	1.54	1.61	1.31	1.34	1.16	1.25	1.18	2.24
Dy	7.47	6.66	3.61	3.63	7.47	8.32	8.97	7.13	6.81	6.88	7.56	6.82	11.65
Ho	1.37	1.23	0.68	0.69	1.4	1.57	1.63	1.32	1.13	1.36	1.49	1.28	1.95
Er	3.42	3.25	1.71	1.81	3.57	4.02	4.24	3.28	2.83	3.7	4.02	3.31	4.83
Tm	0.44	0.41	0.2	0.21	0.46	0.47	0.51	0.42	0.35	0.47	0.53	0.43	0.66
Yb	2.83	2.61	1.37	1.12	2.88	3.08	3.27	2.53	2.3	3.19	3.48	2.72	4.14
Lu	0.39	0.37	0.2	0.18	0.41	0.46	0.48	0.36	0.35	0.47	0.52	0.39	0.55
Y	35.1	34.9	18.3	27.9	38.5	40.3	44.8	34.6	30.3	36.2	37.7	33.2	44.7
∑REE	286.24	270.55	132.34	170.33	275.86	318.29	333.4	277.22	563.88	194.32	207.74	243.56	433.57
∑LREE	224.35	211.81	101.19	128.83	210.79	248.23	256.99	217.29	508.37	133.71	143.57	186.22	347.4
∑HREE	61.89	58.74	31.15	41.5	65.07	70.06	76.41	59.93	55.51	60.61	64.17	57.34	86.17
∑LREE/∑HREE	3.625	3.606	3.248	3.104	3.239	3.543	3.363	3.626	9.158	2.206	2.237	3.248	4.032

∑LREE = ∑LREE(La–Eu) and ∑HREE = ∑HREE(Gd–Lu + Y).

Heishitou in Weining County, is located at east longitude 104°00′20″E and northern latitude 26°48′16″N. The following formations were mapped along the field transect from south to north: the Maokou Formation, Emeishan Basalt Formation, Xuanwei Formation and Feixianguan Formation. In total, 13 samples were collected with numbers CSD-1 to 13, including the units of the first to third lithologic members of the Emeishan Basalt Formation. The analytical results are shown in Table 1. The Emeishan Basalt Formation supplied materials for the overlying Xuanwei Formation (Yang et al., 2008; Yang et al., 2011).

On this section, the Emeishan Basalt Formation, which is approximately 500 m thick, was discomformably sandwiched between the Maokou Formation below and the Xuanwei Formation above (Fig. 3). Three eruption cycles can be distinguished among the Emeishan Basalts according to their basalt layers and sedimentary deposits (Members 1, 2, 3). The first cycle consists of compacted and blocky black basalts interbedded with medium felsic tuffaceous gray muddy shale, in which columnar jointing was developed. The second eruption cycle consists of gray and black thick-layered basalt, with no columnar jointing, typically occurring in thick-layers, and the surface was grayish green after weathering. The third eruption cycle is represented by volcanic ash, black tuffaceous basalt, and basalt with almond-shaped vesicles. The uppermost part of the basalt formation is a layer of purplish red tuff, whose gravels consist of, for instance, basalt, tuff, clay rocks, and aluminum clay rocks.

3. Field geological profile mapping

Six transects (located at Lufang, Maojiaping, Zhangsigou, Fuchu, Diaoshuiyan and Longdongshan) crossed portions of the Xuanwei Formation enriched in rare earth elements and were designed and measured in the field according to their sequences and vertical distribution features (Fig. 1). Related samples were collected on the sections according to the petrologic features of the sedimentary sequences, with a sampling distance between 1 and 2 m, while in case of a single petrologic layer thinner than 1 m, one sample was collected. The petrologic features and thickness of each segment were recorded, and the section map was edited accordingly.

3.1. Lufang—geological profile mapping

This site, located at Xiaohecun village (Lufang), Heishitou Town, Weining County, is at geographical coordinates of east longitude 104°02′05″ and north latitude 26°49′59″ (Fig. 4). The mapping results are shown in Fig. 5.

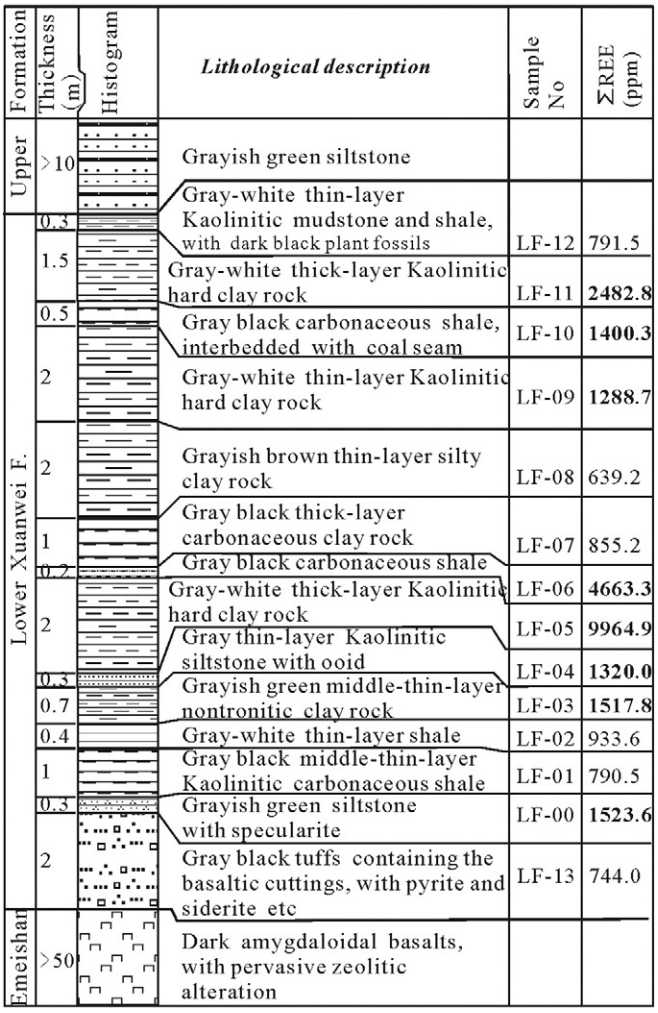

Fig. 5. Stratigraphic column of Lufang.

The geological section is on southeastern side of the Halahe anticline, whose rocks have a dip direction of 320° with angles of 30 to 35°. The Permian Emeishan Basalt Formation and the Xuanwei Formation with a disconformity are present in their sections.

The lower part of the Xuanwei Formation is dominated by gray-white, gray kaolinitic clay rocks interbedded with carbonaceous pelitic

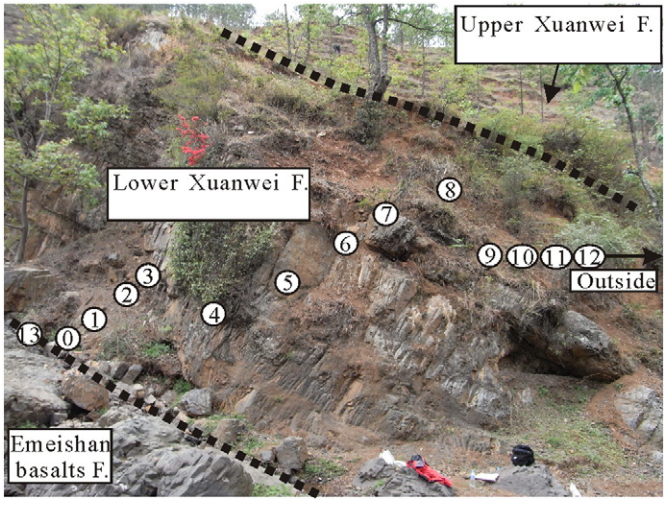

Fig. 4. Photograph of outcrops along the Lufang profile.

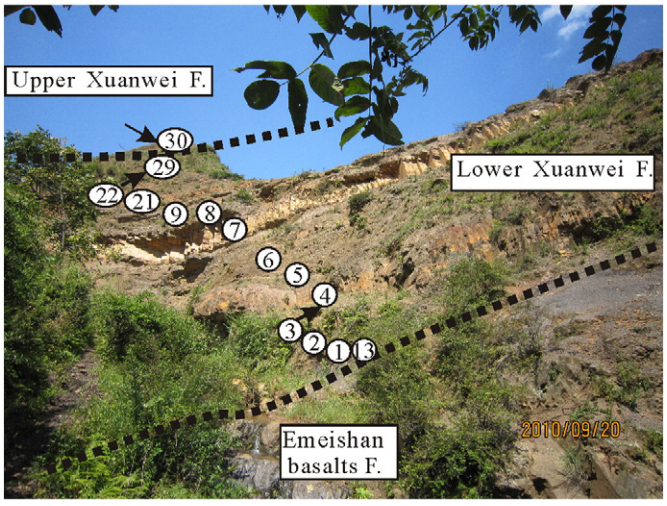

Fig. 6. Photograph of outcrops along the Maojiaping profile.

shales, coal seams, tuffaceous sandy shales and siderite aggregates. The upper part of the Xuanwei Formation is dominated by grayish green siltstone, which exhibits typical spherical weathering structures, and also various layers of yellow-brown silty mudstone interbedded with coal seams.

Geological mapping and sample collection started from the unconformity between the Emeishan Basalt and Xuanwei Formations and ended at the contact between the upper and lower parts of the Xuanwei Formation. In total, 14 samples were collected with intervals of approximately 15 m of strata thickness. The highest REE content is 9965 ppm (Fig. 5, LF-05), the lowest is 639 ppm, and the average value of ∑REE is approximately 2065 ppm. The petrologic characteristics of all samples control the degree of enrichment of rare earth elements. For example, the kaolinitic hard clay rock has the highest content of REEs, followed by the carbonaceous muddy shale, and the silty mudstone, while tuffaceous shale exhibits the lowest content of REEs.

The petrologic characteristics of the profile are as follows: the lowest part is composed of tuff containing black basalt (euhedral pyrite and siderite, etc.), grayish green specularite-containing siltstone, a black thin layer of kaolinitic carbonaceous shale and gray-white thin-layered shale. The middle part consists of brown-green nontronite hard clay rock interbedded with thin-layered kaolinitic ooid-containing silty shale, gray-white thick-layered kaolinitic hard clay rock, and also black carbonaceous shale. The upper part is composed of gray-brown thin-layered silty clay rock, gray-white thin-layered kaolinitic clay rock and is interbedded with thin-layered black carbonaceous shale, gray-white thick-layered kaolinitic hard clay rock and gray-white thin-layered kaolinitic muddy shale.

The above sedimentary units are rhythmically graded from sandstone and clay rock to shale, in which the gray-white thick-layered kaolinitic hard clay rock is the richest unit in terms of REEs. Two thick layers, approximately 4 m thick, of gray-white or gray thick-layered kaolinitic hard clay rock outcrop and consist of REE-enriched layers because they are resistant to weathering.

3.2. Maojiaping—geological profile mapping

The Maojiaping site is near the Heishitou Town in Weining County with geographical coordinates of east longitude 104°01′49″ and north latitude 26°48′50″ (Fig. 6). The mapping results are shown in Fig. 7.

Geologically, this section is on the south-southern side of the Halahe Syncline, and this sequence has a dip direction of 340° and a dip angle of 20–25°. The Permian Emeishan Basalt Formation and the Xuanwei Formation are bounded by parallel unconformities.

The lower part of the Xuanwei Formation is dominated by gray-white, gray kaolinitic clay rock and shale and is also interbedded with carbonaceous argillaceous shale, coal seams, tuffaceous sandy shale and siderite aggregate. The upper part of the Xuanwei Formation is dominated by grayish green siltstone. There are typical spherical weathering structures present, and numerous layers of yellowish-brown silty mudstone interbedded with coal seams.

Field mapping and sampling started from the parallel unconformity between the Emeishan Basalt Formation and the Xuanwei Formation, and proceeded to the contact between the upper and lower parts of the Xuanwei Formation. The sampling interval was 17.5 m of sequence thickness, and a total of 20 samples were collected, of which the highest content of REE is 4713 ppm (Fig. 7, MJP-13) and the lowest is 359 ppm, with an average of ∑REE = 1817 ppm. The grayish green thin layer of clay rock and aluminum shale contained the highest REEs, followed by the kaolinitic hard clay rock and carbonaceous argillaceous shale, and the silty and tuffaceous argillaceous shale has the lowest content of REEs.

The petrological characteristics can be summarized as follows: the lower part is a layer of grayish green nontronite hard clay rock (Fig. 7, MJP-05) exhibiting compact cryptocrystalline textures and plate structures with some fine flake crystalline structures and high content of

Formation	Thickness (m)	Histogram	Lithological description	Sample No	∑REE (ppm)
Upper	>10		Grayish green siltstone	MJP-30	**1047.4**
Lower Xuanwei F.	0.5		Grey black pelitic shale	MJP-29	359.6
	1		Grey black carbonaceous shale	MJP-28	**1192.6**
			Grayish green pelitic shale	MJP-27	335.6
	0.8		Grey black carbonaceous shale	MJP-26	**1123.6**
	0.5		Grey black carbonaceous shale	MJP-25	734.4
			Black carbonaceous shale	MJP-24	684.9
	3		Grey black carbonaceous shale	MJP-23	**2438.4**
			Gray carbonaceous mudstone	MJP-22	766.2
			Gray-white thick-layer kaolinitic hard clay rock	MJP-21	**1032.1**
	0.5		Gray-white Kaolinitic shale	MJP-09	**2960.0**
	1		Gray thin-layer kaolinitic shale interbedded with black carbonaceous strip	MJP-08	**1510.6**
	2		Gray-white thin-layer kaolinitic shale	MJP-07	**1317.5**
	3		Grey black thin-layer carbonaceous shale	MJP-06	623.0
	1		Grayish green middle-thin-layer nontronitic clay rock	MJP-05	726.7
	2		Gray middle-thick-layer aluminum clay rock	MJP-04	**2506.0**
	1		Grey black carbonaceous shale	MJP-03	**1825.9**
	1.5		Grey black carbonaceous shale	MJP-02	500.2
			Gray-white aluminum shale	MJP-01	**3967.6**
	0.5		Grayish green mudstone	MJP-13	**4712.9**
Emeishan	>50		Dark amygdaloidal basalts, with pervasive zeolitic alteration		

Fig. 7. Stratigraphic column of Maojiaping.

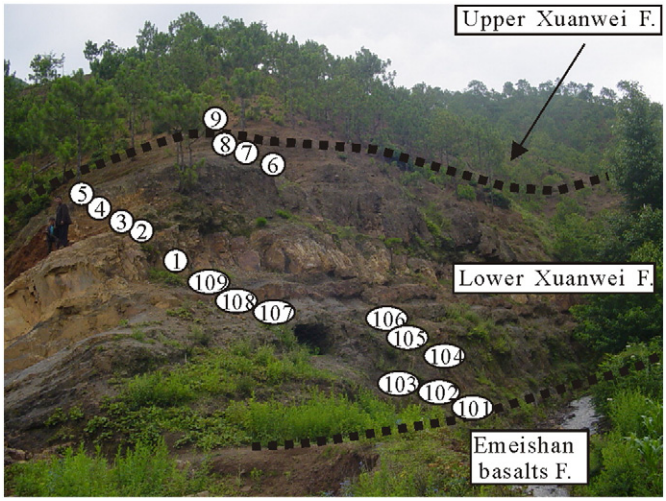

Fig. 8. Photograph of outcrops along the Zhangsigou profile.

iron. This type of minerals normally appears in the lower part of the weathering crust as a weathering and decomposition product of mafic rocks. The underlying layer is dominated by aluminum clay rocks with abundant boehmite (Fig. 7, MJP-04), indicating a high degree of weathering. The middle and upper parts are layers of gray-white kaolinitic hard clay rocks. Other rocks are grayish green thin-layered clay rock with some purplish red tuff layers 0.1–2.0 m in thickness, and grayish green silty mudstone. In comparison, the upper part is thinner in single layers and has more abundant plant fossils, changes faster in terms of petrologic properties and is higher in carbonaceous components than the lower part.

The REE-enriched rocks in the study area can be classified into three units (Fig. 7): the first is on the bottom part of the section, being a thin layer of mudstone and shale 1 m in thickness. The second is in the lower part of the section, being aluminum clay rock and carbonaceous shale 3 m in thickness. The third is in the middle section, dominated by gray-white kaolinitic hard clay rock approximately 6.5 m thick. In addition, the black thin-layered carbonaceous shale also has high a concentration of REEs.

3.3. Zhangsigou—geological profile mapping

The Zhangsigou site is geographically located near the Heishitou Town, with geographical coordinates of east longitude 104°01′40″ and north latitude 26°48′28″ (Fig. 8), and the field mapping are shown in Fig. 9.

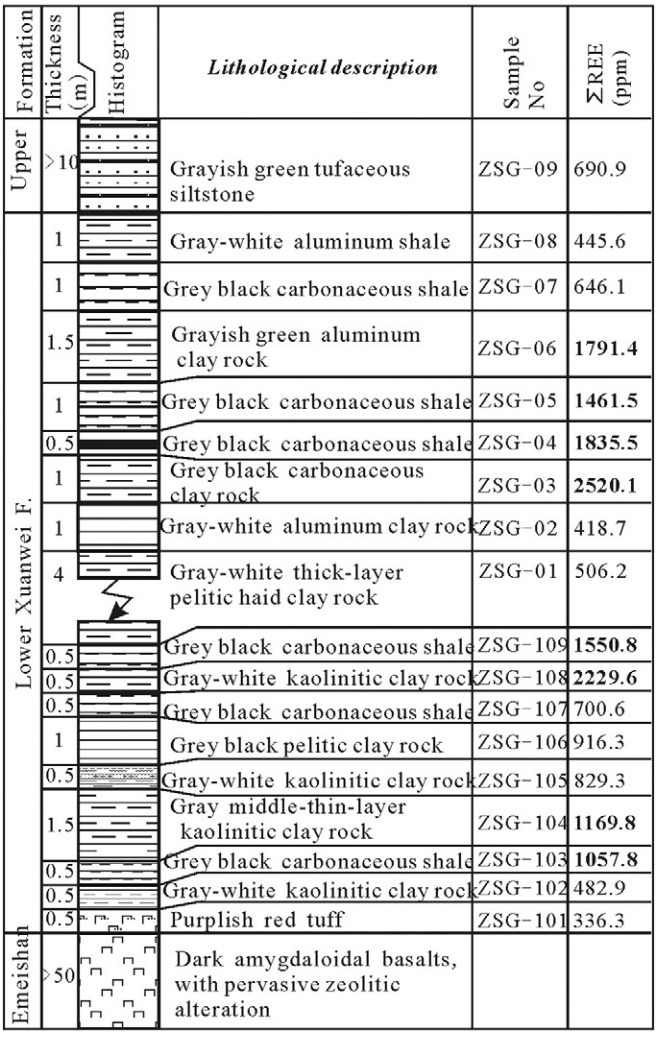

Fig. 9. Stratigraphic column of Zhangsigou.

This section is on the southern side of the Halahe syncline, and has a dip direction of 350° and dip angles of 20–25°. The Permian Emeishan Basalt Formation and Xuanwei Formation are outcropped with a parallel unconformity.

The lower part of the Xuanwei Formation is dominated by gray-white or gray kaolinitic clay rocks and shales interbedded with carbonaceous argillaceous shale, coal seams, tuffaceous sandy shale and siderite aggregates. The upper part of the Xuanwei Formation is dominated by grayish green siltstone and various layers of yellow-brown silty mudstone interbedded with coal seams. The uppermost unit of the section is a layer of gray-green tuffaceous siltstone with distinct spherical weathering and is the boundary between the middle and upper parts of the Xuanwei Formation.

Field mapping and sampling was begun from the parallel unconformity between the Emeishan Basalt Formation and Xuanwei Formation, and proceeded to the contact between the upper and lower parts of the Xuanwei Formation. The sampling interval was 19 m in thickness, and 18 samples were collected in total, of which the highest content of REE is 2520 ppm and the lowest is 336 ppm, with an average $\sum$REE of 1088 ppm.

The petrologic features of the section are as follows: the lower part is dominated by black carbonaceous shale interbedded with gray-white thin-layered kaolinitic clay rock, together forming a layer approximately 5 m in thickness that is enriched with REEs. The middle part is an approximately 5 m thick layer of gray-white kaolinitic hard clay rock with a lower REE content. The upper part is dominated by black thin-layered carbonaceous shale and clay rocks, consisting of a layer approximately 6 m thick that is enriched with REEs. Some layers of carbonaceous clay rocks bear compact cryptocrystalline texture and massive structure; their fractures form a seashell pattern with clear edges and corners, probably indicating high in silica content.

There are no volcanic rocks or regional hydrothermal alteration occurring in the vicinity of the section, but there is one layer of tuffaceous clay rock in the section bottom that contains abundant siderite, some of which exists as a coating of pyrite, indicating other regional hydrothermal processes (Zhang et al., 2010a,b). There are good outcrops of gray-white kaolinitic hard clay rocks (Fig. 8) with sharp differences in petrology, although they are close to the Maojiaping section. There is a layer of purplish red tuff approximately 0.5 m thick in the section bottom overlying the unconformity above the Emeishan Basalt Formation.

3.4. Northern Fuchu—geological profile mapping

This site is north of Fuchu Town in Hezhang County with geographic coordinates of east longitude 104°17′30″ and north latitude 27°10′07″ (Fig. 10), the results of our geological mapping are shown in Fig. 11.

This section is on the northwestern side of the Fuchu syncline and has a dip direction of 120° and dip angles of 15–20°. The Permian Emeishan Basalt Formation and Xuanwei Formation are outcropped with a parallel unconformity. There is layer of purplish red silty–sandy tuff approximately 3 m thick overlying the unconformity. Approximately 10 m of petrologic section was covered with Quaternary sediments in the profile. The sedimentary thickness of the lower part of the Xuanwei Formation in this section is approximately 35 m, being clearly thicker than the sections of Lufang, Maojiaping, and Zhangsigou. There is no distinct marking rock of gray-white thick-layered kaolinitic hard clay rock; instead, grayish green and grayish yellow siltstone and mudstone dominate, and interbedded black carbonaceous shale and siltstone are also present.

The field geological mapping begins with the disconformity between the Emeishan Basalt Formation and Xuanwei Formation, and ended on the contact plain between the upper and lower parts of the Xuanwei Formation. The strata are approximately 35 m thick, and 14 samples were collected. Their highest REE content is 2763 ppm (Fig. 11) and the lowest is 248 ppm, of which 4 samples contain REE > 1000 ppm.

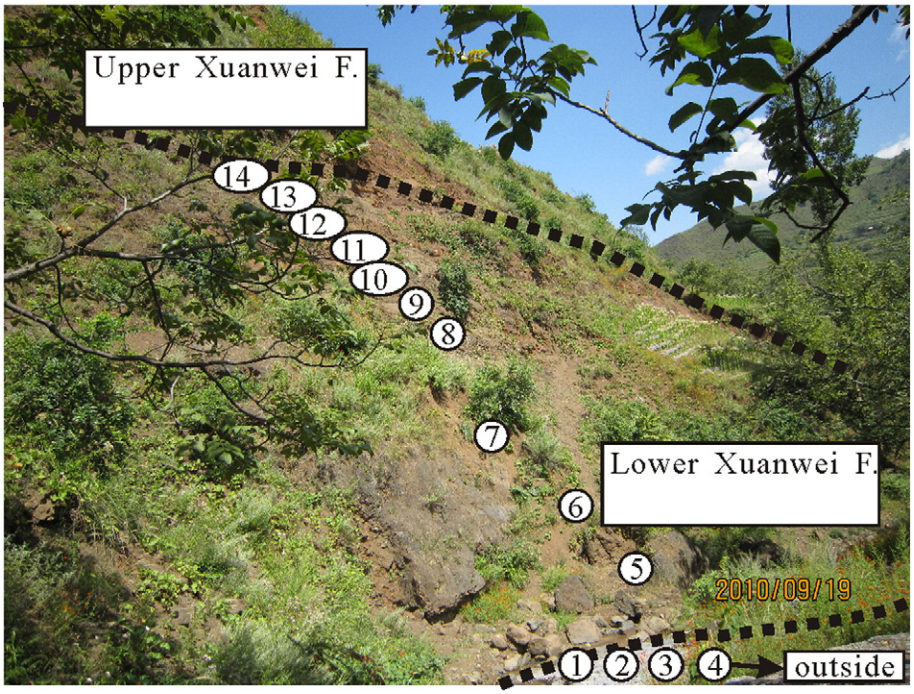

Fig. 10. Photograph of outcrops along the northern Fuchu profile.

The REE-enriched layers (in order of REE enrichment from high to low) are gray-white kaolinitic clay rock, black carbonaceous shale, and silty-tuffaceous shale.

The petrology of the lower part of the section is dominated by silty mudstone and/or shale, including purplish red silty–sandy tuff, brown-reddish silty mudstone, gray-white thin-layered silty kaolinitic shale, purplish red tuffaceous sandstone, and reddish-brown silty mudstone. The middle part consists of gray-white kaolinitic clay rock turned red after oxidation, gray-white middle- and thin-layered kaolinitic clay rock interbedded with black carbonaceous clay rock, and also gray-white kaolinitic clay rock that contains plant fossils. The upper part is dominated by black carbonaceous shale and coal seams, including black thin-layered carbonaceous shale; the black shale bears middle-thin-layered hard silty mudstone and is interbedded with white middle-thin-layered kaolinitic clay rock.

3.5. Diaoshuiyan—geological profile mapping

This site is near the Jinzhong Town in Weining County with geographical coordinates of east longitude 104°24′38″ and north latitude 26°40′40″ (Fig. 12); the mapping results are shown in Fig. 13.

This section is on the northern side of the Diaoshuiyan syncline, and has a dip direction of 170° and dip angles of 15–20°. The Permian Emeishan Basalt Formation and Xuanwei Formation are outcropped with a parallel unconformity (Fig. 12). There is a layer of purplish red silty–sandy tuff approximately 3 m thick above the unconformity.

The lower part of the sedimentary Xuanwei Formation is approximately 10 m thick, which is clearly thicker in comparison with other sections such as Lufang, Maojiaping and Zhangsigou. There are no typical gray-white thick layers of kaolinitic hard clay rocks; instead, there are silty mudstones and sandstones bearing basaltic and tuffaceous clasts and are covered by the upper part of the Xuanwei Formation, which includes carbonaceous clay rock and siltstone interbedded with coal seams. The thickness of a single coal layer is usually over 1 m.

The field geological mapping began from the unconformity plain between the Emeishan Basalt Formation and the Xuanwei Formation, and ended on the contact between the upper and lower parts of the Xuanwei Formation. The sampled strata were approximately 10 m thick, and 5 samples were collected. Their highest REE content is 1023 ppm (Fig. 13) and the lowest is 89.1 ppm, of which just one sample contained REE > 1000 ppm. Because the REE-enriched thick layer of kaolinitic clay rock is absent in this section, the REE contents are always very low in the silty shale and tuffaceous shale. In other words, the enrichment of REE is closely related to petrological properties.

3.6. Longdongshan—geological profile mapping

This site is located at the Longdongshan Town in Hezhang County, and the entire upper and lower parts of the Xuanwei Formation were sampled and analyzed, aiming to understand the distribution characteristics of REE in the formation. In terms of lithology, there is a substantial amount of gray-white kaolinitic clay rock, and the strata is dominated by grayish green and grayish yellow siltstone and mudstone interbedded with black carbonaceous shale and siltstone. Whole-rock geochemical analysis indicated that the grade of REE ore was not good, as only a few samples had REE > 1000 ppm.

Their petrological properties and REE contents yielded some geological information. The outcrop sequence of Xuanwei Formation at Longdongshan is dominated by siltstones and sandstones interbedded with thin-layered gray-white kaolinitic clay rocks and carbonaceous shales; the REE contents of the bulk rocks are not high, mostly in a range of 300–600 ppm, and the highest content is 3700 ppm with a thickness of just 0.2 m. Because the relative content of silt and sand is higher, the REEs are generally lower compared to the other locations.

4. Petrology and mineralogy

Several representative samples were selected for mineralogical analysis, including polarizing light microscopy, scanning electron microscopy and X-ray diffraction on the rock slices, of which the important analyses included micro-mineralogical structures and semi-quantitative analysis of mineralogy.

Experimental methods: the samples from Maojiaping and Zhangsigou were sliced and polished into thin sections, then observed

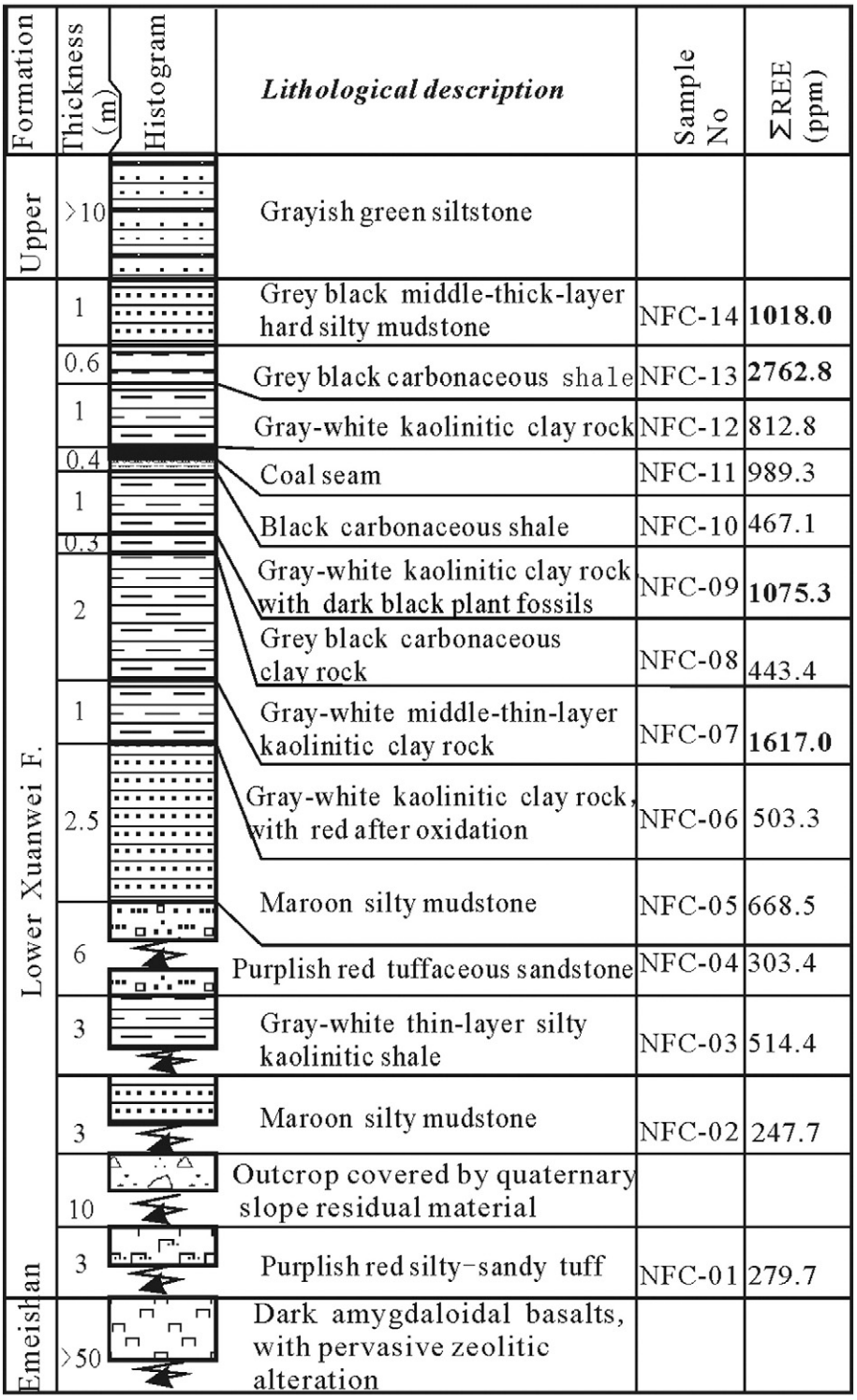

Fig. 11. Stratigraphic column of the northern Fuchu profile.

under an optical microscope. In addition, 22 samples were selected for powder crystal X-ray diffraction analysis at the State Key Laboratory of Deposit Geochemistry, the Institute of Geochemistry, Chinese Academy of Sciences in Guiyang. The mineral contents were semi-quantitatively calculated using the K-value method (Mordberg et al., 2000). The maximum dynamic density of the machine is 2200, and the operation was under standard conditions at 40 kV and 20 mA using Cu-Kα radiation. The oriented samples were scanned over an interval of 2–60° (2θ) at a scanning speed of 10°/min for every 0.04° (2θ).

At the same time, 23 samples were selected from the Maojiaping and Lufang sections for scanning electron microscopy (SEM) analysis at the China University of Geosciences (Beijing) State Key Laboratory of Geological Processes and Mineral Resources. The instrument used was a HITACHI S-450 and HITACHI HUS-5GB under conditions of

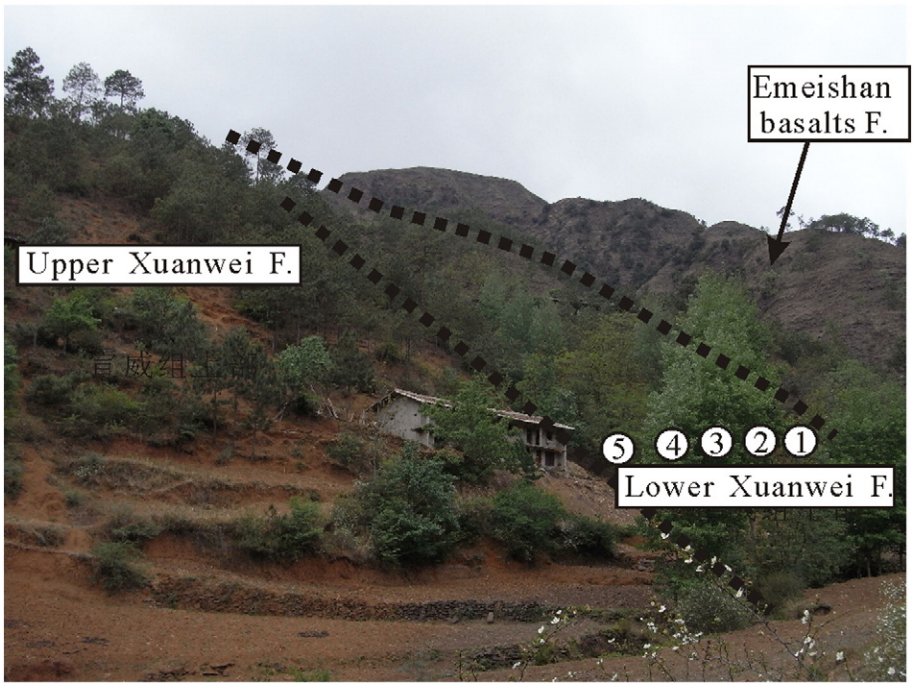

Fig. 12. Photograph of outcrops along the northern Diaoshuiyan profile.

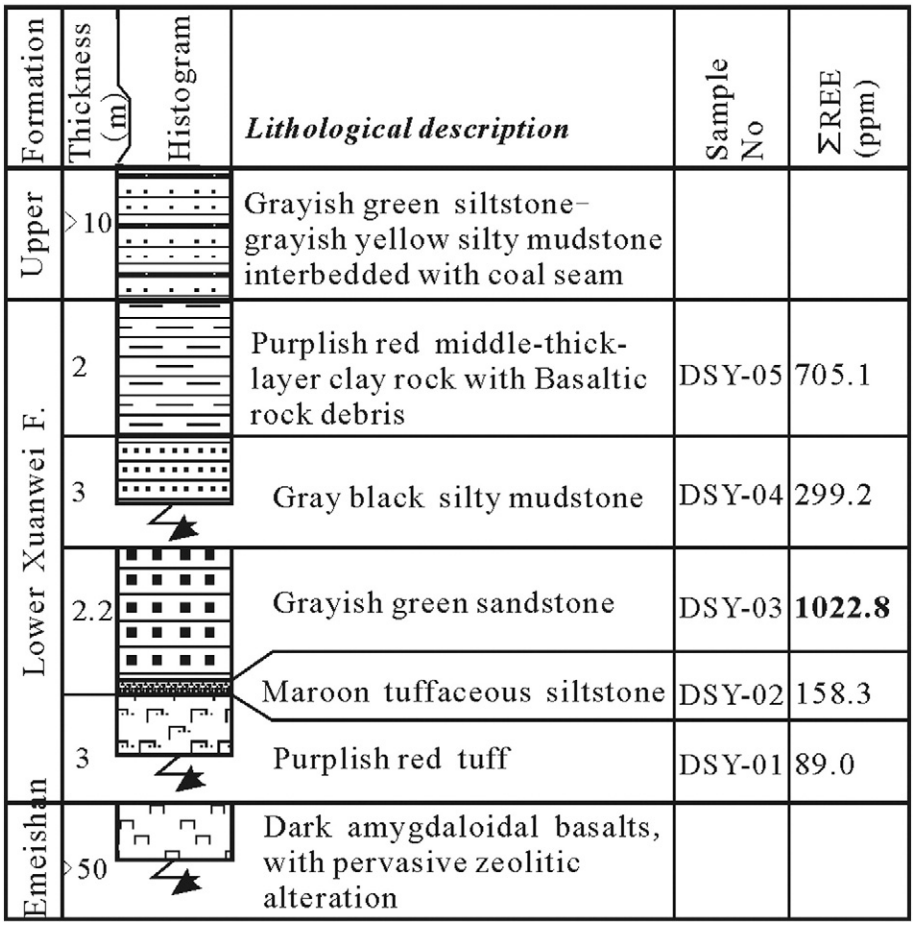

Fig. 13. Stratigraphic column of Diaoshuiyan.

25 kV, 21 ± 0.5 °C with a moisture of 46 ± 1%. The sub-micro status of clay minerals, their correlation to other types of minerals, and the semi-quantitative contents were obtained through XRD and SEM analysis.

4.1. Petrological characteristics

Rocks denomination: based on the sedimentary characteristics, the rocks can be classified into thick-, middle- and thin-layered clay rocks, siltstone, mudstone and shale. Regarding the mineral composition, the rocks can be then divided into kaolinitic, carbonaceous, nontronitic (gray-green), silty, siliceous and tuffaceous clay rocks, etc.

The gray-white kaolinitic hard clay rock is dominated by kaolinite (Fig. 14a), whereas the black kaolinitic hard clay rock is dominated by nontronite (Fig. 14b). There are more carbonaceous belts (bents) in the kaolinitic hard clay rocks (Fig. 14c), which are always interbedded with tuffaceous sandstone (Fig. 14d). However, the carbonaceous shale is always interbedded with clay rock, showing a layered sedimentary texture (Fig. 14e). Clay is the main content of the rocks, and the secondary content includes carbonaceous belts, tuffaceous detritus, feldspar, iron minerals and quartz crystal fragments, and small amounts of bitumen and plant remains (Fig. 14f). The kaolinitic hard clay rocks mostly have block structures, and exhibit less horizontal bedding (having more sedimentary silt particles).

Based on microscope observation, the white siliceous-aluminum mudstone and shale kept the residual ash structures (Fig. 14g), whereas the gray-white carbonaceous shale kept much of the basalt detritus. This detritus is often shown as irregular rough and uneven edges and island-like structures affected by dissolution. There are chalcopyrite particles in the clay rocks (Fig. 14h), and also some tuff fragments and plant fossils (Fig. 14i). It is speculated that the material composition and structural textures of the rocks have continental-sourced sedimentary features. The sources were closely related to the Emeishan Basalts and were influenced by tectonic activity after diagenesis of the sediments, and also some alteration by latter hydrothermal fluids.

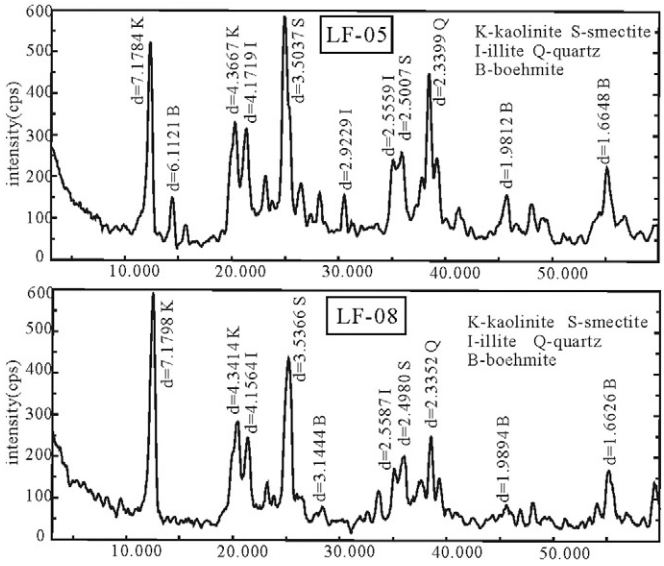

Fig. 15. XRD analyses of samples.

4.2. Mineralogy

4.2.1. Power X-ray diffraction

Power X-ray diffraction (XRD) showed that the crystalline minerals and amorphous minerals (Fig. 15) are all simple in composition, dominated by kaolinite, and secondly included montmorillonite and illite. Some samples contain less boehmite, and commonly contain

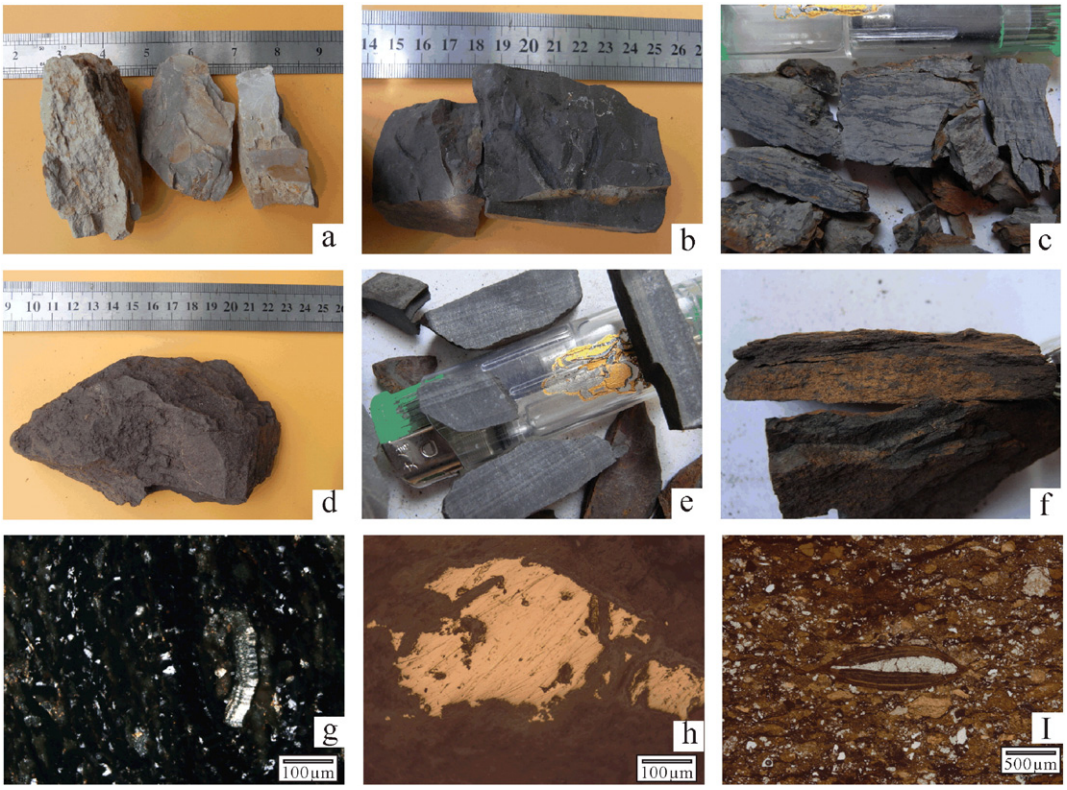

Fig. 14. Structures and textures of samples. a—Gray-white kaolinitic claystone; b—grayish black carbonaceous mudstone interbedded with banded bitumen; c—grayish middle-thin layered mudstone interbedded with banded organic matter; d—purple tuffaceous sandstone; e—grayish black siltstone with horizontal bedding; f—grayish black iron-bearing laminated shale sandstone; g—feldspar with polysynthetic twin; h—chalcocitization; i—plant fossil.

Table 2
Major element (in %) and trace element (in ppm) concentrations of the samples in profile.

Sample texting	NFC-02	NFC-03	NFC-04	NFC-05	NFC-06	NFC-07	NFC-08	NFC-09	NFC-10	NFC-11	NFC-12	NFC-13	NFC-14	LF-00	LF-01	LF-02	LF-03	LF-04
SiO_2	30.91	40.1	35.41	32.7	37.26	41.83	22.53	32.02	20.46	20.28	28.7	35.52	37.25	32.37	22.5	36.54	22.83	41.48
Al_2O_3	24.44	33.27	21.54	26.93	31.15	35.65	24.94	29.81	22.33	22.23	28.35	30.47	32.66	27.04	20.73	31.21	21.39	35.66
Fe_2O_{3T}	25.6	2.16	24.03	20.98	7.87	1.02	36.04	12.86	26.38	26.72	19.19	0.99	3.4	20.21	41.76	11.44	38.85	3.74
CaO	0.08	0.15	0.06	0.01	0.01	0.04	0.01	1.54	0.05	1.29	2.94	0.29	0.07	0.21	0.09	0.18	1.14	0.09
MgO	0.36	0.35	0.34	0.4	0.4	0.3	2.31	0.89	0.74	1.31	1.09	0.32	0.35	1.67	2.67	0.75	2.96	0.37
Na_2O	0.05	0.06	0.04	0.06	0.07	0.1	0.07	0.11	0.05	0.05	0.09	0.1	0.12	0.09	0.04	0.08	0.07	0.1
K_2O	0.09	0.05	0.26	0.45	0.09	0.46	0.03	0.05	0.27	0.14	0.13	0.07	0.09	0.09	0.02	0.11	0.04	0.1
TiO_2	5.04	7.06	5.79	4.08	6.46	4.98	3.56	6.69	6	4.39	3.48	5	7.53	2.82	2.17	3.92	2.34	2.26
MnO	0.04	0.02	0.05	0.02	0.01	<0.01	0.12	0.03	0.03	0.09	0.07	<0.01	0.01	0.06	0.13	0.03	0.17	0.01
P_2O_5	0.231	0.07	0.132	0.15	0.188	0.264	0.139	1.943	0.242	1.719	2.458	0.639	0.179	0.212	0.115	0.098	0.066	0.046
LOl	11.6	14.75	10.55	12.65	14.7	14.35	8.52	12.4	21.9	21.6	11.9	24.5	16.55	13.6	7.92	14.35	8.47	14.7
CIA*	100.94	99.23	99.35	99.10	100.71	99.71	100.67	105.74	100.51	107.43	100.89	102.57	100.02	99.56	100.12	98.91	91.16	99.09
La	38.7	102	53.7	109.5	88.4	364	91.9	145	86.3	140	92.4	607	200	219	123.5	168	154.5	112.5
Ce	85.4	162	116	259	194	640	171	257	185	328	200	1090	398	592	339	357	547	199
Pr	9.05	19	12.8	28.5	17.75	88.7	19.15	30.8	20.9	52	31.3	145	55.6	58.3	27.2	29.8	66.1	33.1
Nd	35.7	65.3	45.9	101.5	61.8	300	62.4	116	70.9	251	157.5	515	198	192	83.2	85.4	284	137
Sm	9.88	13.9	10.1	21.7	13.85	53.4	12	46.5	12.65	61.9	58.4	81.5	26.9	27.5	13.25	15.45	69.4	40.5
Eu	2.92	4.07	2.73	4.84	3.61	9.21	2.4	15.9	2.62	12.05	16.95	18.8	5.09	5.56	2.25	2.79	7.77	7.8
Gd	9.71	14.6	8.31	17.3	14.4	30.2	10.15	74	8.55	35.1	53.1	49.7	14.4	30.2	13.85	18.2	51.7	65.4
Tb	1.52	2.8	1.31	2.91	2.37	3.84	1.8	12.2	1.59	3.77	6.5	6.47	2.35	7.04	3.29	4.5	7.02	13.15
Dy	7.86	16.55	7.35	16.55	13.25	18.65	10.4	63.4	9.98	16.85	28.9	32.9	14.65	46.3	22.5	29.3	37.2	82.8
Ho	1.45	3.34	1.46	3.59	2.73	3.53	2.21	11.3	2.21	2.84	4.76	6.43	3.21	10.15	5	6.34	8.07	18.8
Er	3.7	9.24	3.84	9.96	7.48	8.74	6.14	25.5	6	6.72	9.97	16.5	9.07	26.4	15.1	17.55	22.5	52.7
Tm	0.51	1.3	0.51	1.52	1.11	1.22	0.93	3.04	0.86	0.87	1.11	2.15	1.29	3.82	2.43	2.58	3.26	6.96
Yb	3.37	7.94	3.27	9.61	7.2	7.39	5.78	16.4	5.44	5.23	5.71	12.05	8.33	22.9	16.05	16.3	20.2	39.3
Lu	0.51	1.22	0.46	1.51	1.11	1.1	0.85	2.29	0.84	0.81	0.79	1.86	1.25	3.45	2.43	2.42	3.14	6.02
Y	37.5	91.2	35.7	80.6	74.3	87.1	46.3	256	53.3	72.2	145.5	177.5	79.9	279	121.5	178	236	505
∑REE	247.78	514.46	303.44	668.59	503.36	1617.08	443.41	1075.33	467.14	989.34	812.89	2762.86	1018.04	1523.62	790.55	933.63	1517.86	1320.03
∑LREE	181.65	366.27	241.23	525.04	379.41	1455.31	358.85	611.2	378.37	844.95	556.55	2457.3	883.59	1094.36	588.4	658.44	1128.77	529.9
∑HREE	66.13	148.19	62.21	143.55	123.95	161.77	84.56	464.13	88.77	144.39	256.34	305.56	134.45	429.26	202.15	275.19	389.09	790.13
∑LREE/∑HREE	2.747	2.472	3.878	3.658	3.061	8.996	4.244	1.317	4.262	5.852	2.171	8.042	6.572	2.549	2.911	2.393	2.901	0.671
Ce/Ce*	1.036	0.828	1.005	1.053	1.107	0.809	0.923	0.871	0.989	0.855	0.834	0.834	0.856	1.189	1.326	1.131	1.184	0.738
Eu/Eu*	1.309	1.253	1.308	1.095	1.121	0.980	0.955	1.147	1.095	1.104	1.338	1.272	1.097	0.844	0.728	0.725	0.567	0.640
LREE enrichment flat		+	+	+	+	+	+		+			+	+	+	+	+	+	
MREE enrichment	+							+		+	+							
HREE enrichment																		+

Sample	LF-05	LF-06	LF-07	LF-08	LF-09	LF-10	LF-11	LF-12	LF-13	DSY-01	DSY-02	DSY-03	DSY-04	DSY-05	MJP-01	MJP-02	MJP-03	MJP-04
SiO_2	35.73	34.51	41.21	24.43	39.95	37.66	26.53	40.5	22.27	29.99	33.11	39.22	31.47	31.86	39.28	43.02	39.55	30.07
Al_2O_3	37.95	30.97	36.21	22.93	33.26	31.87	45.94	34.91	21.17	22.62	26.17	27.03	25.38	24.19	32.16	38.80	33.69	47.42
Fe_2O_{3T}	4.81	8.63	3.24	29.6	2.44	0.39	7.16	4.77	41.17	28.76	18.34	9.11	22.79	21.9	4.40	0.92	2.56	2.06
CaO	0.07	0.04	0.04	0.49	0.21	0.09	0.03	0.04	0.13	0.14	0.17	0.28	0.55	0.31	0.14	0.06	0.03	0.01
MgO	0.55	0.87	0.37	1.77	0.34	0.21	0.54	0.38	2.43	0.27	0.3	0.67	0.31	0.38	0.37	0.27	0.22	0.36
Na_2O	0.16	0.15	0.11	0.06	0.07	0.07	0.1	0.09	0.04	0.01	0.02	0.03	0.04	0.02	<0.01	<0.01	0.01	<0.01
K_2O	0.14	0.65	0.24	0.11	0.06	0.22	0.05	0.03	0.02	0.1	0.07	0.38	0.11	0.07	0.16	0.15	0.19	0.16
TiO_2	4	2.32	2.22	4.14	6.85	1.33	4.98	3.57	2.29	5.31	7.05	4.52	5.62	5.71	7.55	1.08	1.95	3.84
MnO	0.03	0.03	0.01	0.1	0.01	<0.01	0.03	0.01	0.12	0.03	0.01	0.02	0.03	0.2	0.02	0.01	0.03	0.01
P_2O_5	0.626	0.243	0.054	0.388	0.153	0.031	0.235	0.07	0.178	0.123	0.22	0.261	0.357	0.465	0.424	0.036	0.106	0.160
LOl	14.3	19.75	15.15	14.25	14.95	27.7	13.35	14.05	8.7	11.1	12.85	16.7	12.1	12.9	15.00	15.45	20.30	14.15
CIA*	102.59	98.60	98.95	99.22	99.42	98.63	100.63	99.76	100.49	99.63	100.42	98.74	98.72	101.86	101.81	99.48	99.93	100.37
La	2690	202	104	82.7	242	54	530	148.5	130.5	17.2	36.7	209	45.4	161	1030	86.3	289	472
Ce	4510	598	193.5	194	458	215	1045	266	243	30.1	57.7	413	96.9	277	1630	123	571	770
Pr	521	163.5	28.7	27.6	58.2	41.5	127	29.5	21.4	3.9	6.55	47.3	12.8	43.4	169	17.9	76.6	115.5
Nd	1345	890	93.9	115.5	198	208	369	92.9	61.7	15.1	22	150.5	53	154	530	69.9	266	367
Sm	132	309	21.7	29.4	34	80.6	58.1	21.8	11.95	3.31	4.8	25.2	13	20.5	73.20	17.95	45.90	55.10

Eu	18.15	32.8	3.47	5.12	5.4	10.6	8.3	3.26	2.67	0.92	1.26	4.92	4.65	4.65	13.05	3.37	5.33	8.33
Gd	88.7	256	27.7	26.6	28.2	79	50.8	24.9	17.15	3.1	4.12	16.8	11.4	9.02	81.7	22.4	45.5	67.1
Tb	16.9	51	8.45	4.3	5.24	16.95	9.27	4.93	4.16	0.38	0.61	3.07	1.72	1.26	10.7	3.92	7.84	13.3
Dy	99.5	328	60.5	22.9	32.5	112.5	46.6	28.5	29	2.1	3.31	18.8	8.64	5.97	52.3	20.7	53.8	87.6
Ho	21.2	67.3	12.95	4.25	7.18	24.1	8.18	5.73	6.59	0.38	0.63	3.77	1.55	0.85	10.3	3.6	13.8	19.1
Er	61.9	189	34.9	10.65	20.5	72.3	20.2	15.3	19.2	1.01	1.51	10.15	3.71	1.77	28.6	8.16	46.3	56.4
Tm	9.65	28.8	5.11	1.49	3.03	11.95	2.85	2.37	2.89	0.15	0.25	1.66	0.54	0.25	3.68	0.94	7.50	8.53
Yb	63.8	190	31.9	8.98	16.5	83.5	18	15.6	18.55	0.88	1.46	10.65	3.11	1.49	20.20	5.73	49.50	53.40
Lu	10.15	27.9	4.48	1.3	2.46	13.3	2.54	2.26	2.76	0.13	0.21	1.55	0.43	0.12	2.87	0.83	7.86	7.72
Y	377	1330	224	104.5	177.5	377	187	130	172.5	10.4	17.2	106.5	42.4	23.9	312	115.5	340	405
∑REE	9964.95	4663.30	855.26	639.29	1288.71	1400.30	2482.84	791.55	744.02	89.06	158.31	1022.87	299.25	705.18	3967.60	500.20	1825.93	2506.08
∑LREE	9216.15	2195.3	445.27	454.32	995.6	609.7	2137.4	561.96	471.22	70.53	129.01	849.92	225.75	660.55	3445.25	318.42	1253.83	1787.93
∑HREE	748.8	2468	409.99	184.97	293.11	790.6	345.44	229.59	272.8	18.53	29.3	172.95	73.5	44.63	522.35	181.78	572.1	718.15
∑LREE/∑HREE	12.308	0.890	1.086	2.456	3.397	0.771	6.187	2.448	1.727	3.806	4.403	4.914	3.071	14.801	6.596	1.752	2.192	2.490
Ce/Ce*	0.859	0.633	0.803	0.912	0.876	0.885	0.915	0.907	1.023	0.834	0.834	0.943	0.911	0.752	0.869	0.708	0.871	0.749
Eu/Eu*	0.729	0.512	0.613	0.805	0.766	0.583	0.671	0.611	0.799	1.262	1.245	1.038	1.678	1.408	0.738	0.730	0.512	0.596
LREE enrichment flat	+				+		+	+		+	+	+		+	+		+	+
MREE enrichment				+									+			+		
HREE enrichment		+	+			+			+									

Sample	MJP-05	MJP-06	MJP-07	MJP-08	MJP-09	MJP-10	MJP-11	MJP-12	MJP-13	MJP-21	MJP-22	MJP-23	MJP-24	MJP-25	MJP-26	MJP-27	MJP-28	MJP-29
SiO_2	29.96	33.54	40.76	33.62	39.65	43.04	30.59	36.56	35.56	42.61	42.38	32.44	30.50	25.20	30.21	27.53	37.56	41.56
Al_2O_3	25.81	23.20	33.32	29.53	34.73	37.87	26.12	34.27	28.8	35.69	36.87	27.32	25.58	21.69	25.42	15.47	8.95	19.11
Fe_2O_{3T}	19.08	17.85	4.78	16.15	1.33	1.29	21.57	8.76	10.83	0.72	0.68	18.34	18.49	34.45	19.77	33.28	26.35	15.52
CaO	1.34	0.39	0.11	1.17	0.03	0.03	0.05	0.02	0.12	0.08	0.10	0.21	0.60	0.13	0.21	1.30	5.74	1.11
MgO	1.49	1.21	0.29	0.90	0.30	0.22	0.24	0.36	0.53	0.18	0.23	0.58	1.32	2.03	0.83	1.26	1.28	1.42
Na_2O	0.01	<0.01	<0.01	<0.01	<0.01	<0.01	<0.01	0.05	0.01	0.01	0.01	0.01	<0.01	0.01	<0.01	0.03	0.03	0.01
K_2O	0.32	0.58	0.21	0.05	0.04	0.09	0.06	0.16	0.17	0.02	0.21	0.32	0.29	0.12	0.31	0.49	0.2	0.5
TiO_2	5.42	4.21	3.21	3.12	6.97	1.57	5.86	2.39	6.81	4.74	3.48	1.34	5.19	2.50	3.16	2.86	1.30	4.16
MnO	0.08	0.07	0.07	0.05	0.01	0.01	0.03	0.01	0.02	0.01	0.01	0.44	0.07	0.35	1.05	0.56	0.92	0.14
P_2O_5	0.937	0.490	0.183	1.107	0.268	0.042	0.484	0.136	0.429	0.100	0.067	0.226	0.378	0.090	0.158	0.192	3.391	0.226
LOl	13.70	16.90	15.45	12.50	14.75	14.70	13.20	15.6	15.15	14.25	14.95	17.15	15.90	11.65	18.10	16.85	12.50	14.50
CIA*	97.89	99.23	99.98	101.56	101.54	99.82	103.93	100.10	102.16	100.16	99.29	99.26	98.02	99.23	98.62	86.17	77.60	90.38
La	92.4	109.5	236	66.8	660	28.6	445	241	873	208	122	363	106.5	123.5	209	60.1	114	59.4
Ce	220	221	407	273	1310	119	983	430	1505	400	219	901	235	271	444	121	293	118.5
Pr	29.9	27.4	55.4	39.3	156.5	12.35	147.5	58	151	44.8	25.7	106.5	27.8	29.2	53.1	13.85	46.9	14.5
Nd	132.5	102.5	185	285	494	72.2	566	210	581	146.5	87.4	380	109	99.5	198	49.1	267	56.2
Sm	39.60	19.45	32.30	153.00	63.90	25.90	104.00	46.5	96.4	22.20	20.30	61.40	22.00	17.20	24.80	8.41	115.50	12.75
Eu	9.73	5.02	8.73	32.6	9.05	4.45	23	4.62	16.45	3.42	3.16	6.61	3.92	2.81	3.6	1.79	24.6	2.76
Gd	41.9	20	38.9	150	56.4	23.9	68.6	29.8	93.4	26.3	24	61.7	19.65	17.5	22.8	7.92	90.7	10.55
Tb	5	3	6.44	18.95	6.98	3.25	8.65	6.14	17.15	4.75	5.37	11.4	3.38	3.23	3.72	1.5	9.91	1.8
Dy	22	16.6	42.8	87	36.6	16.8	39.5	40	114.5	28.1	38.4	71.6	22	22.7	23.2	10.1	39.4	11.4
Ho	3.75	3.19	7.98	12	5.93	2.65	5.04	8.22	25.7	4.32	6.59	11.8	3.91	4.03	4.13	1.74	4.87	2.01
Er	9.77	8.84	25.2	30.8	18.7	7.33	13.8	22.4	69.4	11.75	19.4	32.9	11.15	12.5	13	5.22	10.65	5.77
Tm	1.33	1.19	3.91	4.00	2.79	1.01	1.62	3.58	9.65	1.54	2.87	4.54	1.60	1.94	1.94	0.72	1.10	0.76
Yb	8.54	7.33	24.10	23.70	17.95	6.23	10.90	21.8	48.3	8.74	16.75	26.20	9.14	12.00	12.60	4.79	6.59	4.96
Lu	1.29	1.06	3.82	3.51	2.76	0.94	1.48	3.19	6.95	1.25	2.33	3.79	1.42	1.82	1.78	0.74	0.95	0.78
Y	109	77	240	331	118.5	95.8	85.2	201	1105	120.5	173	396	108.5	115.5	108	48.7	167.5	57.5
∑REE	726.71	623.08	1317.58	1510.66	2960.06	420.41	2503.29	1326.25	4712.90	1032.17	766.27	2438.44	684.97	734.43	1123.67	335.68	1192.67	359.64
∑LREE	524.13	484.87	924.43	849.7	2693.45	262.5	2268.5	990.12	3222.85	824.92	477.56	1818.51	504.22	543.21	932.5	254.25	861	264.11
∑HREE	202.58	138.21	393.15	660.96	266.61	157.91	234.79	336.13	1490.05	207.25	288.71	619.93	180.75	191.22	191.17	81.43	331.67	95.53
∑LREE/∑HREE	2.587	3.508	2.351	1.286	10.103	1.662	9.662	2.946	2.163	3.980	1.654	2.933	2.790	2.841	4.878	3.122	2.596	2.765
Ce/Ce*	0.942	0.916	0.808	1.104	0.926	1.384	0.862	0.826	0.927	0.939	0.886	1.037	0.981	1.025	0.957	0.952	0.881	0.917
Eu/Eu*	1.047	1.117	1.072	0.945	0.662	0.786	1.181	0.537	0.762	0.617	0.624	0.471	0.829	0.711	0.665	0.964	1.053	1.045
LREE enrichment flat		+	+		+		+	+	+	+		+	+	+	+	+		+
MREE enrichment	+			+		+											+	
HREE enrichment											+							

(continued on next page)

Table 2 (*continued*)

Sample texting	NFC-02	NFC-03	NFC-04	NFC-05	NFC-06	NFC-07	NFC-08	NFC-09	NFC-10	NFC-11	NFC-12	NFC-13	NFC-14	LF-00	LF-01	LF-02	LF-03	LF-04
Sample	ZSG-01	ZSG-02	ZSG-03	ZSG-04	ZSG-05	ZSG-06	ZSG-07	ZSG-08	ZSG-09	ZSG101	ZSG102	ZSG103	ZSG104	ZSG105	ZSG106	ZSG107	ZSG108	ZSG109
SiO_2	33.18	41.95	41.53	28.02	29.05	37.60	35.27	36.06	42.79	18.89	21.93	44.1	27.44	43.38	24.45	42.38	36.62	22.64
Al_2O_3	29.64	17.56	35.46	27.22	25.86	32.37	27.50	17.63	30.07	14.75	18.93	35.45	25.65	37.38	24.86	37.13	32.84	52.84
Fe_2O_{3T}	20.24	22.84	1.70	24.24	23.43	3.43	12.26	22.77	2.52	39.57	41.84	4.21	32.77	2.32	30.26	1.01	5.81	2.19
CaO	0.08	0.68	0.01	0.01	0.03	0.11	0.25	0.37	0.21	0.42	0.37	0.15	0.12	0.2	0.06	0.03	0.08	0.07
MgO	1.34	2.49	0.27	1.00	0.80	0.27	0.53	1.35	0.64	1.02	2.51	0.39	2.04	0.28	1	0.18	0.54	0.2
Na_2O	0.01	0.03	<0.01	0.01	<0.01	0.01	<0.01	0.01	0.01	0.03	0.02	0.1	0.03	0.12	0.04	0.06	0.11	0.08
K_2O	0.04	0.64	0.11	0.06	0.15	0.28	0.55	0.35	0.37	0.04	0.04	0.09	0.09	0.08	0.12	0.06	0.83	0.06
TiO_2	1.89	3.08	2.47	2.17	2.79	4.41	4.67	3.18	5.83	3.55	4.86	1.29	1.03	1.27	2.91	4.43	1.64	6.74
MnO	0.09	0.10	0.01	0.10	0.07	0.01	0.08	0.14	0.02	1.41	0.39	0.02	0.12	0.03	0.09	0.01	0.04	0.01
P_2O_5	0.041	0.349	0.236	0.219	0.171	0.234	0.236	0.374	0.107	0.112	0.272	0.043	0.062	0.076	0.143	0.102	0.188	0.235
LOl	11.55	8.82	16.70	15.40	15.95	19.75	16.70	16.15	15.75	18.85	8.26	13.8	9.32	14.65	14.6	14.2	21.1	14.15
CIA*	99.64	93.89	101.17	101.59	100.69	100.13	98.21	99.03	98.23	96.17	99.49	98.80	99.16	98.77	100.15	100.07	97.70	100.45
La	57.8	78	457	320	271	316	116.5	75.7	135.5	40.83	77.53	60.14	184.1	47.95	152.6	92.53	243.7	127.2
Ce	201	156.5	871	531	518	691	241	156.5	275	58.2	87.4	329.9	560.8	142.2	231.5	199.8	443.5	727.8
Pr	22.3	18.05	96.9	72.5	64.9	87.1	29.3	18.55	29.6	12.68	19.55	42.48	54.17	20.05	36.65	31.07	70.88	96.43
Nd	91	68.5	302	255	216	320	109.5	72.4	101.5	49.22	75.19	173.63	178.23	94.22	129.84	112.17	273.93	318.09
Sm	19.45	13.00	55.00	60.50	34.40	52.60	16.45	15.30	14.85	11.85	15.06	42.07	22.24	29.51	21.5	20.67	63.87	52.36
Eu	2.69	2.88	6.6	8.65	3.07	6.82	2.84	3.35	3.01	1.82	2.39	4.81	2.24	6.9	2.31	2.3	7.43	8.89
Gd	15.15	10.8	57.7	56.4	29.5	40.6	14.2	12.85	13.7	10.67	15.01	34.96	23.12	45.16	21.72	21.56	78.32	47.64
Tb	2.45	1.63	11.35	10	5.71	6.39	2.37	2.11	2.34	1.61	2.39	5.18	2.77	7.08	3.71	3.41	12.68	5.92
Dy	15	9.63	82.3	65.2	40.8	38.8	15.65	12.85	15.7	9.8	14.4	30.13	15.59	43.89	24.01	21.6	78.59	31.68
Ho	2.45	1.6	15.45	11.35	7.8	6.58	2.87	2.18	2.77	2.24	3.1	7.15	3.38	10.03	5.49	4.71	18.24	6.44
Er	7.24	4.74	49.9	33.7	25.7	21	8.68	5.79	8.42	6.54	8.32	19.28	9.47	29.12	16.26	13.03	52.15	17.23
Tm	1.09	0.67	7.93	4.99	4.15	3.12	1.27	0.82	1.22	1.01	1.22	3.02	1.46	4.38	2.49	1.95	8.19	2.56
Yb	6.66	4.06	48.10	29.90	24.70	19.00	7.47	4.90	7.80	5.89	7.53	17.49	8.87	26.35	15.02	11.17	47.18	15.4
Lu	0.98	0.6	6.93	4.32	3.77	2.94	1.15	0.8	1.17	0.94	1.17	2.83	1.4	4	2.38	1.66	7.3	2.35
Y	61	48.1	452	372	212	179.5	76.9	61.5	78.4	123	152.7	284.8	102	318.5	250.9	163	823.7	90.82
∑REE	506.26	418.76	2520.16	1835.51	1461.50	1791.45	646.15	445.60	690.98	336.30	482.96	1057.87	1169.84	829.34	916.38	700.63	2229.66	1550.81
∑LREE	394.24	336.93	1788.5	1247.65	1107.37	1473.52	515.59	341.8	559.46	174.6	277.12	653.03	1001.78	340.83	574.4	458.54	1103.31	1330.77
∑HREE	112.02	81.83	731.66	587.86	354.13	317.93	130.56	103.8	131.52	161.7	205.84	404.84	168.06	488.51	341.98	242.09	1126.35	220.04
∑LREE/∑HREE	3.519	4.117	2.444	2.122	3.127	4.635	3.949	3.293	4.254	1.080	1.346	1.613	5.961	0.698	1.680	1.894	0.980	6.048
Ce/Ce*	1.241	0.947	0.937	0.791	0.887	0.945	0.937	0.949	0.984	0.577	0.510	1.299	1.271	1.007	0.703	0.836	0.764	1.285
Eu/Eu*	0.686	1.067	0.514	0.651	0.423	0.646	0.816	1.049	0.927	0.711	0.698	0.551	0.433	0.804	0.469	0.478	0.457	0.782
LREE enrichment flat	+	+	+	+	+	+	+	+	+	+	+	+	+		+	+		+
MREE enrichment																		
HREE enrichment														+			+	

∑LREE = ∑LREE(La–Eu) and ∑HREE = ∑HREE(Gd–Lu + Y); $Ce/Ce^* = 2(Ce/Ce_N) / (La/La_N + Pr/Pr_N)$; $Gd/Gd^* = 2(Eu/Eu_N) / (Sm/Sm_N + Gd/Gd_N)$; where N indicates normalized to the NASC (Haskin et al., 1966).
$CIA^* = [(Al_2O_3) / (Al_2O_3 + CaO - 10/3{*}P_2O_5 + Na_2O + K_2O)] \times 100$.

hornblende, pyrophyllite, calcite, dolomite and iron-bearing minerals (the high content of iron might be from nontronite and ripidolite).

There are clear diamond polysynthetic twin-shaped siderites in the samples from the bottom part of the Lufang section. Because of higher contents of amorphous materials, the peaks of XRD spectra are not high and sharp, so it is difficult to calculate the absolute contents of various minerals. Therefore, the amorphous part was deducted, and the relative contents in terms of percentages of crystalline minerals were calculated. The mineral composition thus obtained is just a relative content, but it reflects well the relative abundances of crystalline materials (Table 3).

At the same time, the amorphous materials do not appear to influence the correlations between mineral composition and REE contents in the samples (Table 4). From the correlation analysis of the relative mineral abundances and REE concentrations, it is observed that the contents of REE, LREE, and HREE have positive correlations with montmorillonite, illite, pyrophyllite, and the secondary clay minerals, and also higher positive correlations with boehmite (AlOOH), hornblende and iron-bearing minerals, but a lower correlation with the major mineral kaolinite. The clay minerals such as montmorillonite, illite, and pyrophyllite, are all layer silicates, their crystal structures are normally scale-like and plate-like with high specific surface area, and they typically have interlayer structures, inducing strong absorption capability. Therefore, the positive correlation between REE content and clay minerals (and also boehmite) may indicate that rare earth elements are absorbed as ions in the interlayers and/or inter-particle spaces of clay minerals. The positive correlation with hornblende and iron-bearing minerals may suggest that REE occurs in the remaining minerals that are strongly resistant to weathering; for example, MREE mainly occurred in common hornblende. However, because of the direct measurement of REE status is absent in this study, the above extrapolation is indirect.

4.2.2. SEM analysis

SEM analysis revealed good coarse crystalline structures of kaolinite, which were mostly laminated, with particle sizes near 10 μm, and also some fine irregular flake-like particles of kaolinite (Fig. 16a, b) exhibiting clear sedimentary characteristics. There are small amounts of single laminated kaolinite particles with a false appearance of feldspar (Fig. 16c), showing the features of replacement kaolinite (Yang and Zhang, 1991). There are also some fine flake particles or aphanocrystalline kaolinite aggregates (Fig. 16d, e), probably indicating the sequence of rocks formed and altered by latter hydrothermal fluids. As observed by SEM, fine and small flake-like montmorillonite and burr-like illite often occurred with kaolinite; the weathered remains of tuffaceous fragments and organic matter were also generally observed (Fig. 16f).

The occurrence of organic matter can explain why the carbonaceous mudstone and shale are rich in REE. The study of elemental behavior during weathering of modern basalt showed that organic matter may significantly improve the migration of insoluble elements (Ma et al., 2007). After complexion with organic colloids, the activity of REE will be substantially increased, and these REE will migrate much more easily from the source rocks and then precipitate as the organic colloids decompose (Bau, 1999). The alteration traces of latter hydrothermal fluids on the minerals are clearly observed. These results are quite similar to the results of copper mineralization by previous researchers (Zhu et al., 2003; Li et al, 2004; Zhang et al., 2010a,b). However, there is still insufficient evidence of the occurrence of hydrothermal fluids either during or after diagenesis.

5. Geochemistry

All samples were crushed to powder, with particles smaller than 200 mesh, and the contents of major elements and trace elements were measured using X-ray fluorescence (XRF) and inductively coupled plasma mass spectrometry (ICP-MS), respectively. The laboratory experiments were completed in the ALS Laboratory Group, Mineral Division (Guangzhou).

Measurement of major elements in bulk rocks: after calcination of the powdered sample, 2.000 g of sample was mixed with $Li_2B_4O_7$–$LiBO_2$, placed into an automatic melting instrument, and fused at 1050–1100 °C. The fused melt was removed, and then a glass flat formed after cooling. This flat was measured using XRF for elemental concentrations. The iron content is total iron, and the measurement limit for major elements is over 0.01 wt.%.

Measurement of trace elements: 2.000 g of sample was mixed with $LiBO_2$ and heated at over 1000 °C to melting. After cooling, the mixture was transferred into a solution of nitric acid, which was ready for ICP-MS analysis. The main purpose of this method is to measure concentrations of REE. At the same time, it is also reliable for minor and least-soluble elements such as Ba, Cr, Nb, Rb, Sn, Ta, W, and Zr. The analytical results would only be considered if there were much more elements and/or sulfides present in the samples. The detection limits for the trace elements can be referred to the literature (Zhou et al., 2013). The analytical results for bulk rocks are listed in Tables 1 and 2.

5.1. Major elements

5.1.1. Major elements can be used to indicate the weathering degree of source rocks

Major elements can be used to indicate the weathering degree of source rocks, such as the chemical index of alteration (CIA; Nesbitt and Young, 1982), which is implicated to discuss the rocks in each section. Using the data in Table 2 to make a triangular scatter diagram (Fig. 17), it is clearly shown that all of the measured sections have experienced a similar intensity of weathering, and a clear trend of enrichment of aluminum. The concentration of Al_2O_3 is mostly in the 95–99% range, indicating abundant clay minerals enriched with Al in the rocks.

The samples from the Lufang section are the highest in Al enrichment and are also the richest in REE, indicating that the Ca-, Na-, and K-enriched silicate minerals might be replaced by Al-rich clay minerals during the weathering process. For example, it is normally considered that there is no clear enrichment in TiO_2 (3.92%; cf. Emeishan Basalts, TiO_2 3.84%), whereas Al_2O_3 (28.61%) and Fe_2O_3 (15.38%) become enriched as easily soluble elements such as CaO (0.443%), Na_2O (0.055%), MgO (0.854%), and K_2O (0.242%) become depleted. In the literature, Ti and Zr have been found to be active elements in the tropic zone with extremely intense weathering (Braun et al., 1993; Walter et al., 1995; Patino et al., 2003), and complexing with organic matter will dramatically increase the activity of Al, Zr, Ti, Th and other elements (Viers et al., 1997; Ma et al., 2007). Paleogeographical studies revealed that the present western Guizhou Province used to be located in the low latitude region of the southern hemisphere in the Late Permian epoch, with hot and humid climate, abundant rainfall and thriving plants (Guo, 1991). Thus, it can be speculated that some very strong weathering occurred in this area in the Late Permian epoch that induced washing loss of relatively stable TiO_2. A relative increase of LOI (the average is 14.58%) in the sediments relative to their source rocks could also be a clear tracer for the increase in water during the alteration due to weathering. This type of alteration and replacement may occur much more thoroughly, and the weathering degree should be much deeper.

Regarding the CIA (Nesbitt and Young, 1982), under the same experimental conditions if the minerals in the rocks are all feldspars, the CIA should be 50; if the minerals are biotite, common hornblende and pyroxene, the CIA could be 50–55, 10–30 and 0–10, respectively. Especially for the secondary clay minerals such as kaolinite and gibbsite, their CIA would be 100, and 70–85 for illite and montmorillonite (Nesbitt and Markovics, 1997). Thus, the higher content of iron- and magnesium-materials in the rocks may indicate a lower degree of

Table 3
Results of XRD analyses (%).

Sample no	Kaolinite	Montmorillonite	Illite	Pyrophyllite	Boehmite	Hornblende	Dolomite	Calcite	Quartz	Feldspar	Iron-mineral	Amorphous mineral	∑REE
LF-05	66.57	3.82	2.15	2.46	15.24					1.62	8.41	✓	1320.0
LF-06	81.62	6.10	4.16			3.12			5	x		✓	9964.9
LF-10	94.81	3.26	1.31				0.62			x	x	✓	1400.3
LF-13	80.08	7.86	2.92		1.14	2.08	1.42	0.82	1.22	2.46	x	✓	744.0
MJP-01	87.31	6.24	1.06						4.23	1.16	x	✓	3967.6
MJP-03	92.86	1.62		0.36	x				5.16			✓	1825.9
MJP-04	50.41	3.62	1.13	x	41.82				2.16	0.86	x	✓	2506.0
MJP-05	83.68	5.25	3.86	2.74	3.15		1.32			x		✓	726.7
MJP-06	77.48	5.19	3		1.14	0.62			10.22	1.1	1.25	✓	623.0
MJP-07	89.55	2.03	1.06	0.51		0.62		x	3.72	1.66	0.85	✓	1317.5
MJP-08	88.73	5.86		3	0.91	0.62	x		x	x	0.88	✓	1510.6
MJP-09	87.8	5.63	1.42		x	1.66			2.88		0.61	✓	2960.0
MJP-10	92.55	2.16	1						3.77	0.52	x	✓	420.4
MJP-13	85.4	6.82	1.73	x	0.58	0.6	0.92	0.7	0.86	1.36	1.05	✓	4712.9
MJP-21	85.97	3.15	x	2.46					6.18	2,24	x	✓	1032.1
MJP-22	89.51	1.33	0.74						4.92	2.88	0.62	✓	766.2
MJP-24	89.72	3.91		1.11	x	0.45			1.95	2.86	x	✓	684.9
MJP-25	83.57	5.66	1.83	2.24	0.82	1.72	0.34	1.15	1.25	1.42	x	✓	734.4
MJP-26	87.99	5.25	0.84	1.72		1.06		x	1.9	1.24	x	✓	1123.6
MJP-28	34.16	7.1	1.42		x	2.76	2.82	1.62	48.23	1.34	2.82	✓	1192.6
MJP-29	40.82	3	0.9	x	0.45	0.86	0.52	1	49.33	x	3.12	✓	359.6
MJP-30	39.4	3.16	1.25			x			54.33	1.86	x	✓	1047.4

✓ — Detected the amorphous mineral nature; x — detected the crystalline minerals, but lower levels failed to determine the mineral names; % — mineral percentage is content of crystalline state in whole rock for calculating benchmark, but does not include the content of amorphous.

Table 4
Correlation analyses between the relative contents of mineral and the average content of REE.

	Kaolinite	Montmorillonite	Illite	Pyrophyllite	Boehmite	Hornblende	Dolomite	Calcite	Quartz	Feldspar	Iron mineral	∑REE	LREE
Kaolinite	1.000												
Montmorillonite	−0.088	1.000											
Illite	0.127	0.491[a]	1.000										
Pyrophyllite	−0.498	0.767[a]	0.740	1.000									
Boehmite	−0.525	−0.492	−0.381	−0.267	1.000								
Hornblende	−0.342	0.554	0.509	0.342	0.354	1.000							
Dolomite	−0.527	0.588	0.163	[b]	0.605	0.757	1.000						
Calcite	−0.698	0.009	−0.376	[b]	−0.053	0.749	0.645	1.000					
Quartz	−.869[c]	−0.053	−0.195	−0.118	−0.231	0.195	0.415	0.636	1.000				
Feldspar	0.179	−0.149	0.113	−0.203	−0.495	−0.069	−0.024	−0.423	−0.024	1.000			
Iron-mineral	−0.481	−0.058	0.261	0.314	0.947[a]	0.449	0.224	0.655	0.979[c]	−0.163	1.000		
REE	−0.029	0.167	0.179	0.187	0.308	0.294	−0.027	−0.447	−0.282	−0.155	0.763[a]	1.000	
LREE	−0.065	0.116	0.079	0.194	0.299	0.162	0.013	−0.428	−0.270	−0.137	0.808[c]	0.973[c]	1.000
HREE	0.114	0.261	0.439	0.044	0.229	0.413	−0.108	−0.487	−0.223	−0.207	0.100	0.556[c]	0.349

[a] Correlation is significant at the 0.05 level (2-tailed).
[b] Cannot be computed because at least one of the variables is constant.
[c] Correlation is significant at the 0.01 level (2-tailed).

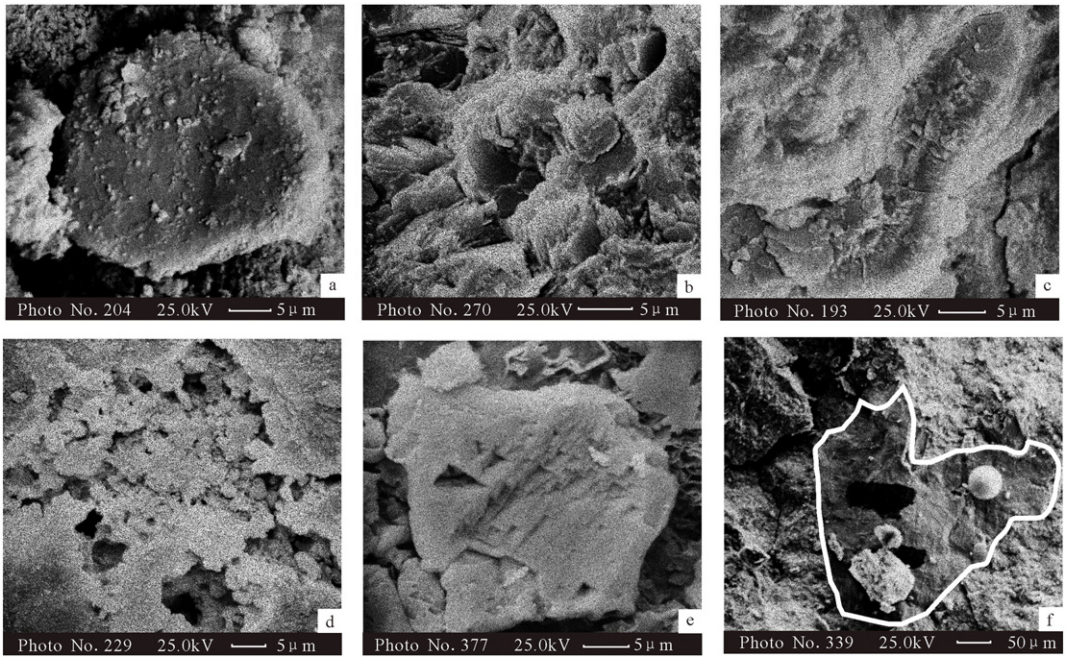

Fig. 16. SEM images of REE ores from the Xunwei Formation. a—Pseudo-hexagonal sheet kaolinite polymer; b—fine flakelet of kaolinite aggregate comprising the primary basic components; c—laminated kaolinite aggregate, feldspathic; d—compact kaolinite together will a little illite and smectite filling in the cavities; e—typical secondary overgrowth structure with triangular pits developed from quartz due to subsequent hydrothermal alteration; f—rock debris, with irregular and altered rim, attached with black bituminous spherical spores.

weathering intensity, whereas the more aluminum-rich minerals in the rocks may indicate a higher degree of weathering. The CIA for the Emeishan Basalts is 38–40, and for the lower part of sediments of the Xuanwei Formation is mostly 95–99, increasing by approximately 30% relative to their source rocks.

5.1.2. Major elements normally reflect the source region of the detrital material in the rocks

Major elements normally reflect the source region of the detrital material in the rocks. By using a typical graphic solution for the other source area of major elements in sandstone–mudstone (Roser and Korsch, 1988), samples from each section were separately put into the diagram (Fig. 18) which showed that most samples studied were located in the region for femic volcanic rocks, and fewer samples were in the region for felsic and neutral volcanic rocks.

Regarding the above XRD and SEM-EDS results (Table 3), it is shown that phenocrysts of quartz fragments occurred. In fact, quartz concentrations were lower in the Emeishan Basalts, so that their sources are not only from the Emeishan Basalts but also partially from the neutral-felsic volcanic rocks erupted in the latter period because there was less felsic magma activity at the time of emplacement of the Emeishan Basalts (Chung and Jahn, 1995). Many researchers believed

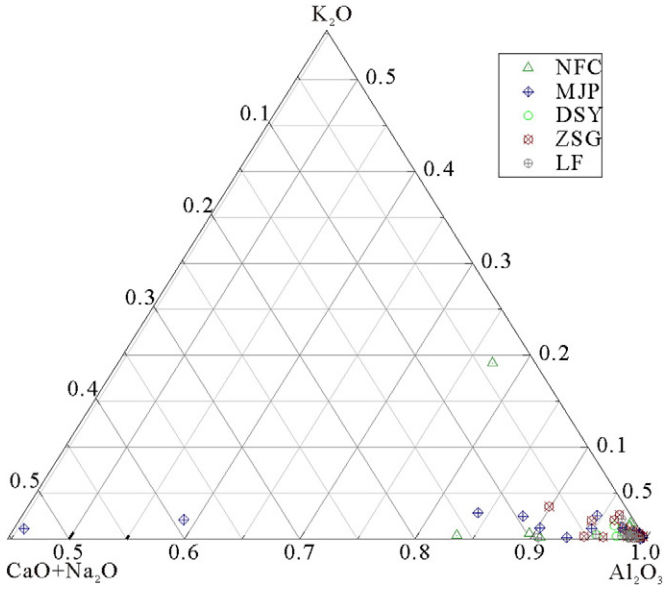

Fig. 17. Triangular Al_2O_3–($CaO^* + Na_2O$)–K_2O plot diagram (Nesbitt and Young, 1982) of investigated samples.

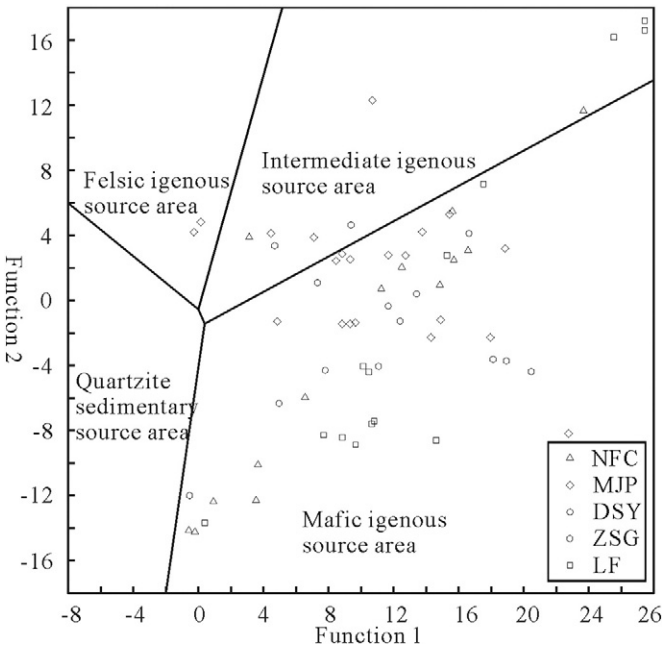

Fig. 18. Discrimination diagram of provenance of sediments (after Roser et al., 1988). Function 1 = −1.773 TiO_2 + 0.60 $7Al_2O_3$ + 0.76 Fe_2O_3T − 1.5 MgO + 0.616 CaO + 0.509 Na_2O − 1.224 K_2O − 9.09; Function 2 = 0.445 TiO_2 + 0.07 Al_2O_3 − 0.25 Fe_2O_3T − 1.142 MgO + 0.438 CaO + 475 Na_2O + 1.426 K_2O − 6.861.

that the latter Permian clastic rocks in the Upper Yangtze area were all sourced from the Emeishan Basalts (He et al., 2003, 2006, 2007). For example, the bauxite in Guangxi Province has been confirmed to have contributions from the Emeishan Basalts (Deng et al., 2010; Liu et al., 2010; Wang et al., 2010). Most likely, the sediments of the lower part of the Xuanwei Formation were originated from the Emeishan Basalt Formation.

5.2. Trace elements

There are different degrees of enrichment of trace elements such as Ga, Cu, Nb, Ta, Zr, and Hf in the rocks, of which the enrichment of Nb, Ta, Zr, and Hf are related to their relatively high stability during the water–rock alteration. However, the enrichment of Ga is conformed to its migration behavior during the surface weathering process because it can be incorporated into Al and Fe oxides during weathering, and can replace Al through isomorphism (Luo et al, 2007). The bulk Ga concentration and relatively high clay mineral contents determined by XRD revealed that the Ga concentration was correlated highly with kaolinite and pyrophyllite, thus this element might replace Al in kaolinite and pyrophyllite through isomorphism during weathering. However, the enrichment of copper should not be induced by the weathering-denudation and sedimentation of basalts, and also should not have originated from contemporaneous lava, but should be formed mainly from the alteration by hydrothermal fluids. The Cu mineralization mainly occurred in the top part and sedimentary interlayers of the Emeishan Basalt Formation, and mostly existed in the form of native copper (Zhu et al., 2003; Li et al, 2011).

5.3. Rare earth elements (REE)

5.3.1. REE concentrations

The ∑REE of the five investigated sections of Lufang, Maojiaping, Zhangsigou, Northern Fuchu, and Diaoshuiyan range from 89.1 to 9965 ppm with an average of 1312 ppm (Fig. 19). Approximately 48% of all samples have over 1000 ppm of REE, and their distribution is not concentrated, whereas the samples with ∑REE of 1000–1500 ppm and 500–1000 ppm are relatively concentrated. The average of ∑LREE (La–Nd) and ∑HREE (Er–Lu + Y) are 980 ppm and 332 ppm, respectively. The ratio of LREE/HREE in the Emeishan Basalts, including the eruptive intervals, is approximately 3.70, whereas the REE deposits in the Xuanwei Formation have a ratio of 2.96, showing that the enrichment of HREE in the REE deposit bodies is higher than that of LREE in the underlying Emeishan Basalts.

5.3.2. Spatial distribution of REE

When we compare the ∑REE contents of each sample with the petrological properties of each section, the following points are observed.

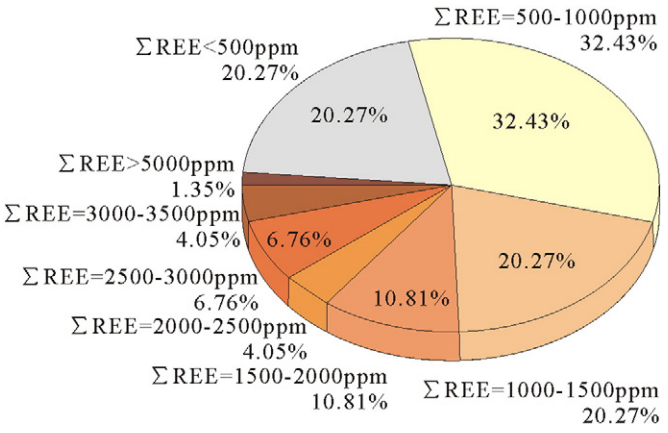

Fig. 19. Pie chart of the contents of REE.

The samples with ∑REE over 1000 ppm are either gray-white kaolinitic hard clay rock or black carbonaceous mudstone and shale (Fig. 20). Compared with XRD results, it will be seen (Table 3) that this type of sample is dominated by kaolinite, montmorillonite, and illite similar to the samples of gray-white thick-layered kaolinitic hard clay rock (approximately 2 m thick) from the Lufang section, where the mineral contents of kaolinite, illite and pyrophyllite are approximately 80% of the whole rock (Fig. 5, LF05).

In the spatial distribution, REE-enriched rocks are mainly distributed as intervals in the lower part of the Xuanwei Formation (Fig. 20). Considering the unconformity between the Xuanwei Formation and the underlying Emeishan Basalts as a reference plane, there are generally two layers of REE enrichment. The first one is found approximately 5 m over the disconformity, and the petrological layer with REE content over 1000 ppm is 3–6 m thick. The second layer is approximately 13 m over the disconformity, and the petrological layer with a REE content over 1000 ppm is also 3–6 m thick. Compared with the Halahe tectonic syncline, the Northern Fuchu section is located in another syncline (the Fuchu syncline) and its strata is thicker, but there are fewer layers of kaolinitic clay rocks, and silty shale and coal seams occur relatively frequently. There is only one layer approximately 3 m thick that is enriched with REE in this section, and the enrichment degree is lower.

5.3.3. REE distribution pattern

Based on the results of all of the 71 samples from 5 sections and the tuffaceous fragments of the Emeishan Basalts for chondrite-normalization (Fig. 21), it is generally shown that the rocks from the lower part of the Xuanwei Formation have similar REE distribution patterns to the Emeishan Basalts. However, there is a large change in total content of REEs with Ce and Eu anomalies. Compared with the Emeishan Basalts, the enrichment of REE is over 10 times higher in the rocks from the lower part of the Xuanwei Formation; most of the samples have negative Ce and Eu anomalies, and fewer samples have positive Ce anomalies.

The ratio of Ce/Ce* was generally lower than unity (Table 2) and was accompanied by weaker positive anomalies. The occurrence of a positive Ce/Ce* anomaly may be caused by the following factors: under

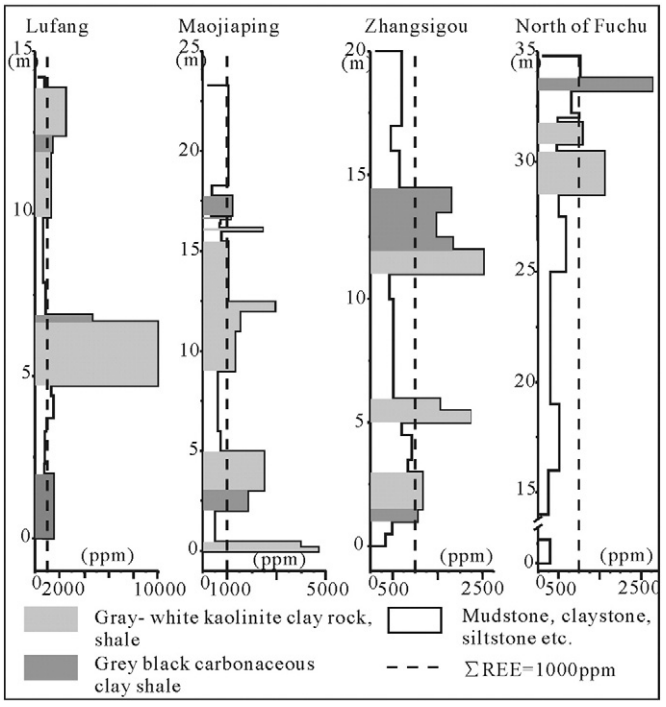

Fig. 20. Correlation of the REE contents with lithology of the samples from different profiles.

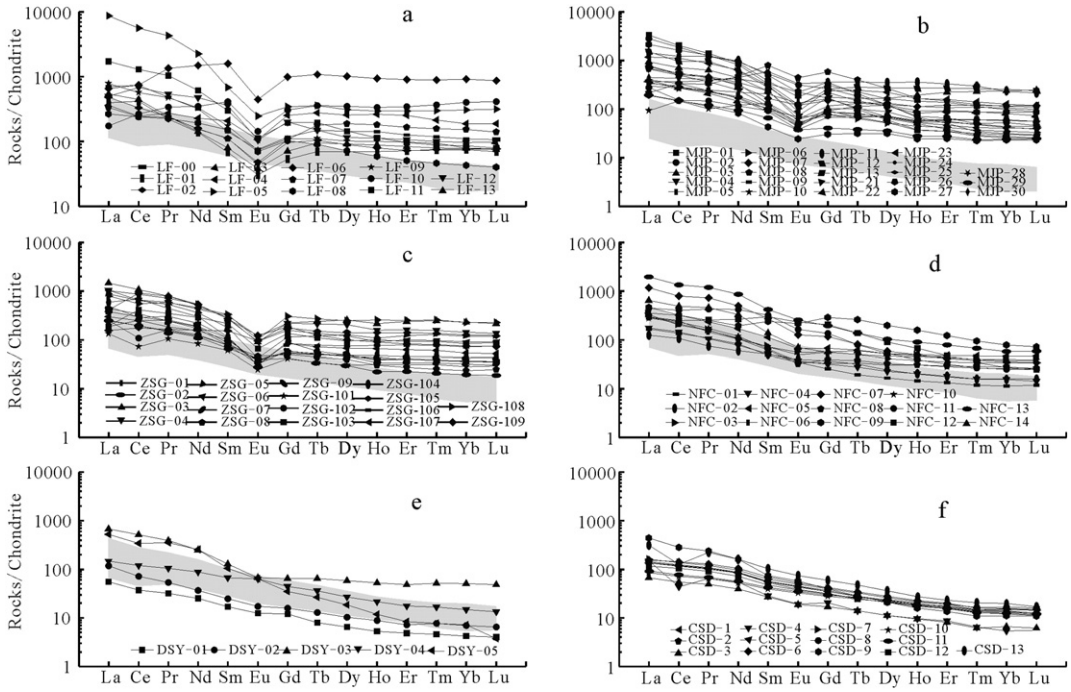

Fig. 21. Chondrite-normalized REE patterns of all samples. (a) Lufang profile (samples from LF-00 to LF-13); (b) Maojiaping profile (samples from MJP-01–MJP-13 and MJP-21–MJP-30); (c) Zhangsigou profile (samples from ZSG-01–ZSG-09 and ZSG-101–ZSG-109); (d) North of Fuchu profile (samples from NFC-01 to NFC-14); (e) Diaoshuiyan profile (samples from DSY-01 to DSY-05); (f) Chushuidong profile of the Emeishan Basalts (samples from CSD-01 to CSD-13); CSD-03, 04, 09 and 13 represent the 4 samples of the eruptive discontinuous surface in the Emeishan basalt; the dashed area represents the chondrite-normalized REE patterns of basalts.
After Zhong et al. (2009).

the surface environment, Ce^{3+} of the basalt is easily oxidized into Ce^{4+}, and the stability of Ce^{4+} is stronger than Ce^{3+} which is possibly fixed in the accessory minerals such as clay minerals. Thus, the enrichment facies of Ce in the weathering sections are mostly Ce^{4+} (Braun et al., 1993), inducing a positive anomaly of Ce/Ce*. This property also indicates that such REE enrichment not only results from a pure sedimentary process (negative anomaly) but is also affected by weathering processes. In addition, strong hydrothermal fluid activity may also induce a positive Ce anomaly (Karakaya, 2009). Therefore, hydrothermal mineralization could be the dominant factor inducing positive Ce anomalies in siderite, chalcopyrite, native copper and other minerals at the bottom of the Xuanwei Formation.

There are similar ratios of samples with positive and negative anomalies of Eu/Eu* (Table 2). The negative anomaly of Eu/Eu* resulted from weathering (Ma et al., 2007), and the positive anomaly probably reflects the weathered fragments produced from medium-felsic rocks as the source rocks (Zhao et al., 1999). In addition, the Emeishan gabbro also exhibited a positive Eu anomaly (Zhong et al, 2009). Laboratory experimentation showed that stable Eu^{3+} was mostly inclined to stay in the leachate at low pH and high oxygen fugacity, and then would transfer to the clay minerals through alteration by latter hydrothermal fluids left with much more Eu^{2+} (Sverjensky, 1984). Therefore, some hydrothermal types of REE deposits (Palacios et al., 1986; Karakaya, 2009) and marine bottom hydrothermal REE deposits (German et al., 1990) often showed positive Eu anomalies. It can be considered through the study of Ce/Ce* and Eu/Eu* characteristics that the REE-enriched layers in the lower part of the Xuanwei Formation might have originated from the Emeishan Basalts, and may also include some addition of medium-felsic magma materials. Their enrichment in REE should be dominated by sedimentation; weathering and latter hydrothermal fluid alteration should be the secondary factors.

Through standardized data processing using NASC northern American shale, the differentiation of REE becomes clearer and can be classified into four types of distribution patterns, including the LREE-enriched, MREE-enriched, HREE-enriched, and flat types (Table 2). The MREE-enriched type of rocks can be explained from the following two aspects: one is the rocks remaining with the common hornblende enriched with MREE as a residue of the source rocks (Prudencio et al., 1993), even if the content is lower; it is also able to significantly influence the content and distribution of REEs (Rollinson, 1993). Another aspect is where alteration of later hydrothermal fluids induced redistribution of REE, especially the enrichment of MREE. Karakaya (2009) discovered REE behavior during hydrothermal fluids alteration where the MREEs of the kaolinitic rocks were enriched by a factor of 5–10 relative to the fresh original source rocks. Therefore, the enrichment of MREE may suggest that alteration by hydrothermal fluids occurred during the latter diagenesis, and the influence of this type of alteration on the whole sequence should be regionally limited area (Nesbitt et al., 1990).

6. Discussion

6.1. Abundance, distribution and resource potential of REE

As discussed above, the observed geological sections and their petrological, mineralogical and geochemical properties are generally described in terms of the abundance distribution features of REEs as follows: (1) REE-enriched layers of rocks are mostly in the lower part of the Xuanwei Formation, mostly being gray-white thick-layered kaolinitic hard clay rocks, followed by black middle-thin-layered carbonaceous clay rock. However, the silty clay rock, tuffaceous clay rock and silty shale are lower in REE. There are some regular features in the petrological layers: from lower to upper on the section, there is a change in petrology from sandstone and clay rocks to shale, to form a sedimentary cycle of REE-enriched layers (Fig. 5). (2) The clay rocks enriched with REE contain crystalline and amorphous minerals. The crystalline minerals are mainly kaolinite and nontronite, followed by montmorillonite, illite, and small amounts of boehmite, and other common minerals

include hornblende, pyrophyllite, calcite, dolomite and some iron-bearing minerals. Variations in the REE could be closely related to mineral compositions. The higher the contents of clay minerals in the rocks, the higher the REE contents generally are in the rocks. There are some positive correlations between the contents of REE, LREE, HREE and montmorillonite, illite, pyrophyllite, etc., and also some positive correlations with boehmite, hornblende, and iron-bearing minerals. However, the correlation with kaolinite is lower. Therefore, it is estimated that most REEs can be adsorbed into the interlayers of clay minerals as cations, and smaller amounts of REEs may occur in the rock fragments. (3) The REE content is over 1800 ppm in REE-enriched layers, which is approximately 2 times higher than the industrial grade of the cation absorbing type of REE deposits in southern China (China Mineral Resources Reserves Committee, 1987).

6.2. REE conditions and enrichment mechanism

Under the surface environment, the elements with strong resistance to weathering include Zr, Hf, Nb, Th, Al, and Ti (Chesworth et al., 1981; Nesbitt and Markovics, 1997), and some of them may change their individual activity (Hill et al., 2000). All REE can be migrated and fractionated to some degree, and strongly enriched in the lower parts of weathered profiles (Balashov, 1964; Nesbitt, 1979). REE dilution and positive Ce anomalies normally occur in the upper part of the weathered layer of basalt as the source rock, and the enrichment of REE, especially the HREE enrichment and negative Eu anomaly, often occurred in the lower part of the basalt (Patino et al., 2003; Ma et al., 2007). Study examples and laboratory simulation already revealed that HREE were much more easily released from the original minerals than LREE, inducing relative enrichment of LREE in the upper part and HREE in the lower part of the weathering profile (Cullers et al., 1973; Nesbitt, 1979; Prudencio et al., 1993). The above study results are helpful for us to analyze and distinguish the chemical status of REE. For example, the results above will be helpful to analyze the chemical status of REE in the study area, such as higher REE rocks at the Lufang, Maojiaping, and Zhangsigou sections, which showed clearly higher enrichments of HREE compared with LREE. It is believed that weathering-washing is a major factor in forming these REE-enriched layers.

For the ion exchange type of rare earth element deposits in southern China (Wu et al., 1990), the granite as a source rock contains REE-bearing accessory minerals that are mostly weakly resistant to weathering, such as bastnaesite, parisite, and gadolinite. Thus, the REE in these minerals mostly occurred as adsorbing ions (Bao and Zhao, 2008). In this study area, REE contents have higher positive correlations with clay minerals, indicating a higher possibility of these REEs being adsorbed on the clay minerals as cations. The XRD results showed that some MREE-enriched samples contain small amounts of common hornblende, suggesting that their MREE might remain in the individual minerals rich in MREE.

The enrichment of REE is controlled by the processes of transportation and deposition of weathered materials. The cations, including Ca^{2+}, Na^{+}, K^{+} and so on, are initially released from the silicate minerals, whereas the stable elements such as Al, Fe, Ga, Hf, Nb, Ta, and Th will remain in the residues. The REEs will be released from the minerals due to their weak resistance to weathering and will migrate with leaching solution, while a portion of the REEs will still remain in the minerals with strong resistance to weathering. Leaching and enrichment of REEs in the weathered crustal materials result in migration over short distances and accumulation in the sedimentary basins (He et al., 2003), the intensity of weathering and the degree of clay formation were enhanced which leads to the formation of extremely REE-enriched clay–siltstone sedimentary layers. The REE-enriched weathering sediments were sustained by a certain degree of hydrothermal alteration during their diagenesis, but their impact on the distribution of REE is generally insignificant.

6.3. REE distribution and sedimentary environments

The chondrite partition of REE-enriched layers has similar features to the Emeishan Basalts (Fig. 21), but there are some large differences in total contents of REEs, and in Ce and Eu anomalies. Total REEs are over 10 times as enriched, indicating that some strong weathering enrichment occurred. The Ce/Ce* ratio was generally lower than unity (= negative Ce anomaly), probably suggesting weathering as an important factor affecting the enrichment of REE. In addition, alteration by hydrothermal fluids could also induce a positive Ce anomaly (Karakaya, 2009). The studied samples exhibit both negative and positive Eu anomalies, suggesting that a negative anomaly might result from weathering (Ma et al., 2007) and a positive anomaly might be due to the addition of medium-felsic magma materials into the weathered sediments (Nesbitt and Markovics, 1997). Therefore, REE-enriched layers should be formed during the migration and sedimentation of ancient weathering crustal materials.

7. Conclusions

The Xuanwei Formation is a series of interbedded shore and ocean-continental sediments. The lower part of this formation is limited in terms of range of iron, bauxite, and copper-mineralization, and most rocks of this formation are not considered to be industrial ore bodies. However, these aluminum carbonaceous clay rocks and/or shales are enriched in REE, Ga, Nb and Zr, the REE content is far higher than the industrial grade residual clays type REE deposits of South China, and the layers are stable in thickness. Although these elements have not been developed to much extent, mainly because their status has not been clearly known, their resources are potentially very impressive and available for economic development once a breakthrough in mineral processing technology is made.

The REE-enriched layers consist of kaolinitic clay rock, and carbonaceous clay rock interbedded with muddy and silty shale, whose materials are mainly sourced from the underlying Emeishan Basalt Formation. The mineral compositions of the rocks are dominated by kaolinite, followed by montmorillonite and illite with a lesser amount of pyrophyllite, boehmite, calcite, etc., and also some phenocrysts of quartz and feldspar as well as an amorphous component. The contents of rare earth elements are mainly in the range of 1500–2500 ppm and are contained in clay minerals as absorbing ions such as illite and pyrophyllite; however, a lesser amount of REE may be contained as individual accessory minerals with a strong resistance to weathering. It can be speculated that the formation of these REE-enriched layers might be related to the migration-sedimentary processes of the weathered-crust materials of the Emeishan Basalt Formation, which may be able to form a new type of sedimentary layer controlling REE deposits.

Conflict of interest

The authors of this article contend without controversy.

Acknowledgments

The research work was financially supported by the Natural Science Foundation of China (41173064; 41273112; 41020124002), the 12th Five-Year Plan project of State Key Laboratory of Ore-deposit Geochemistry, Chinese Academy of Sciences (SKLODG-ZY125-08), and Chinese Academy of Sciences Visiting Professorship for Senior International Scientists to YT (2012T1Z0035). The authors are grateful to Prof. Franco Pirajno and Prof. Yanjing Chen for their helpful suggestions about an early version of this manuscript.

Appendix A. Supplementary data

Supplementary data associated with this article can be found in the online version, at http://dx.doi.org/10.1016/j.oregeorev.2015.07.018. These data include the Google map of the most important areas described in this article.

References

Balashov, Y.A., 1964. The effect of climate and facies on the fractionation of the rare earths during sedimentation. Geochem. Int. USSR 5, 951–968.

Bao, Z., Zhao, Z., 2008. Geochemistry of mineralization with exchangeable REY in the weathering crusts of granitic rocks in South China. Ore Geol. Rev. 33 (3–4), 519–535.

Bau, M., 1999. Scavenging of dissolved yttrium and rare earths by precipitating iron oxyhydroxide: experimental evidence for Ce oxidation, Y–Ho fractionation, and lanthanide tetrad effect. Geochim. Cosmochim. Acta 63 (1), 67–77.

Braun, J.J., Pagel, M., Herbilln, A., Rosin, C., 1993. Mobilization and redistribution of REEs and thorium in a syenitic lateritic profile: a mass balance study. Geochim. Cosmochim. Acta 57 (18), 4419–4434.

Cao, L.L., Zhu, S.H., Wang, J.W., 1994. Origin and genesis of Bayan Obo Fe-REE deposit. Science in China (Series B) 24 (12), 1298–1307 (in Chinese).

Chakhmouradian, A.R., Smith, M.P., Kynicky, J., 2015. From "strategic" tungsten to "green" neodymium: a century of critical metals at a glance. Ore Geol. Rev. 64, 455–458.

Chen, W.Y., Liu, J.R., Wang, Z.G., Zheng, Q.L., 2003. Study on lithofacies palaeogeography during the Permian Emeishan basalt explosion in Guizhou Province. J. Palaeogeogr. 5 (1), 17–28 (in Chinese with English abstract).

Chesworth, W., Dejou, J., Larroque, P., 1981. The weathering of basalt and relative mobilities of the major elements at Belbex, France. Geochim. Cosmochim. Acta 45 (7), 1235–1243.

China Mineral Resources Reserves Committee, 1987. Reference Manual for Manufacture Demand of the Mineral Resources. Geological Publishing House, Beijing, pp. 1–672 (in Chinese).

Chung, S.L., Jahn, B., 1995. Plume–lithosphere interaction in generation of the Emeishan flood basalts at the Permian–Triassic boundary. Geology 23 (10), 889.

Cullers, R.L., Medaris, L.G., Haskin, L.A., 1973. Experimental studies of the distribution of rare earths as trace elements among silicate minerals and liquids and water. Geochim. Cosmochim. Acta 37 (6), 1499–1512.

De Boer, M.A., Lammertsma, K., 2013. Scarcity of rare earth elements. ChemSusChem 6 (11), 2045–2055.

Deng, J., Wang, Q., Yang, S., Liu, X., Zhang, Q., Yang, L., Yang, Y., 2010. Genetic relationship between the Emeishan plume and the bauxite deposits in Western Guangxi, China: constraints from U–Pb and Lu–Hf isotopes of the detrital zircons in bauxite ores. J. Asian Earth Sci. 37 (5–6), 412–424.

Emsbo, P., McLaughlin, P.I., Breit, G.N., du Bray, E.A., Koenig, A.E., 2015. Rare earth elements in sedimentary phosphate deposits: solution to the global REE crisis? Gondwana Res. 27 (2), 776–785.

Fan, H.R., Chen, F.K., Wang, K.Y., Xie, Y.H., Wilde, S., Stair, M., 2002. Zircon U–Pb age of a carbonatite dyke from Bayan Obo REE–Fe–Nb deposit, Inner Mongolia and its geological significance. Acta Petrol. Sin. 18 (3), 363–368 (in Chinese with English abstract).

Geological Team 108, Guizhou Bureau of Geology & Mineral Resources, 1973. Geological Survey Report of the Weining Sheet: Regional Mineral Census Section, pp. 114–115 (in Chinese).

German, C.R., Klinkhammer, G.P., Edmond, J.M., Mura, A., Elderfield, H., 1990. Hydrothermal scavenging of rare-earth elements in the ocean. Nature 345 (6275), 516–518.

Guo, Y.T., 1991. Ecology of the Late Permian Gigantopteridaceous plants in Western Guizhou, China. Coal Geol. Explor. 2, 12–15 (in Chinese with English abstract).

Haskin, L.A., Wildeman, T.R., Frey, F.A., Coliins, A., Keedy, C.R., Haskin, M.A., 1966. Rare earths in sediments. J. Geophys. Res. 71 (24), 6091–6105.

He, B., Xu, Y.G., Chung, S.L., Xiao, L., Wang, Y., 2003. Sedimentary evidence for a rapid, kilometer-scale crustal doming prior to the eruption of the Emeishan flood basalts. Earth Planet. Sci. Lett. 213 (3–4), 391–405.

He, B., Xu, Y.G., Xiao, L., Wang, Y.M., Wang, K.M., Shao, S.L., 2006. Sedimentary responses to uplift of Emeishan mantle plume and its implications. Geol. Rev. 52 (001), 30–37 (in Chinese with English abstract).

He, B., Xu, Y.G., Huang, X.L., Luo, Z.Y., Shi, Y.R., Yang, Q.J., Yu, S.Y., 2007. Age and duration of the Emeishan flood volcanism, SW China: geochemistry and SHRIMP zircon U–Pb dating of silicic ignimbrites, post-volcanic Xuanwei Formation and clay tuff at the Chaotian section. Earth Planet. Sci. Lett. 255 (3–4), 306–323.

Hill, I.G., Worden, R.H., Meighan, I.G., 2000. Geochemical evolution of a palaeolaterite: the Interbasaltic Formation, Northern Ireland. Chem. Geol. 166 (1–2), 65–84.

Hu, R.Z., Tao, Y., Zhong, H., Huang, Z.L., Zhang, Z.W., 2005. Mineralization systems of a mantle plume: a case study from the Emeishan igneous province, southwest China. Earth Sci. Front. 12 (1), 042–054 (in Chinese with English abstract).

Huang, X.H., 1997. The Lufang rare earth deposit in Weining, western Guizhou and its mineralization. Geol. Guizhou 14 (4), 328–333 (in Chinese with English abstract).

Karakaya, N., 2009. REE and HFS element behaviour in the alteration facies of the Erenler Dagl Volcanics (Konya, Turkey) and kaolinite occurrence. J. Geochem. Explor. 101 (2), 185–208.

Kato, Y., Fujinaga, K., Nakamura, K., Takaya, K., Ohta, J., Nakashima, T., Iwamori, H., 2011. Deep-sea mud in the Pacific Ocean as a potential resource for rare-earth elements. Nat. Geosci. 1–5.

Kynicky, J., Smith, M.P., Xu, C., 2012. Diversity of rare earth deposits: the key example of China. Elements 8 (5), 361–367.

Li, J.W., Long, Y.K., Lu, F.Q., 2005. Study on the genesis of weathering crust type REE ore deposit in Jiangmen area, Guangdong, China. West-China Exploration Engineering (9), 101–104 (in Chinese).

Li, H.M., Mao, J.W., Xu, Z.B., Chen, Y.C., Zhang, C.Q., Xu, H., 2004. Copper mineralization characteristics of the Emeishan basalt district in the Yunnan–Guizhou border area. Acta Geosci. Sin. 25 (005), 495–502 (in Chinese with English abstract).

Li, H.M., Mao, J.W., Zhang, C.Q., 2011. Geochemistry of fluid inclusions of the basalt copper deposits in adjacent area of Northeastern Yunnan and Western Guizhou, China. J. Earth Sci. Environ. 33 (1), 14–33 (in Chinese with English abstract).

Liu, T.G., 1985. Geological and geochemical character of Baiyou Ebo dolomite carbonitite. Acta Petrol. Sin. 1 (3), 15–28 (in Chinese with English abstract).

Liu, S.R., Hu, R.Z., Yao, L.B., Zhou, G.F., 2006. Study on the mineral composition of the clastic phosphate in Zhijin phosphate deposits, China. Acta Mineral. Sin. 26 (1), 118 (in Chinese with English abstract).

Liu, X., Wang, Q., Deng, J., Zhang, Q., Sun, S., Meng, J., 2010. Mineralogical and geochemical investigations of the Dajia Salento-type bauxite deposits, western Guangxi, China. J. Geochem. Explor. 105 (3), 137–152.

Luo, T.Y., Dai, X.D., Zhu, D., Tao, Y., Song, X.Y., Zhang, H., 2007. Mineralization of gallium: implication to Emeishan Large Igneous Province. Bull. Mineral. 27 (3–4), 281–286 (in Chinese with English abstract).

Ma, J.L., Wei, G.J., Xu, Y.G., Long, W.G., Sun, W.D., 2007. Mobilization and re-distribution of major and trace elements during extreme weathering of basalt in Hainan Island, South China. Geochim. Cosmochim. Acta 71 (13), 3223–3237.

Mei, M.X., Ma, Y.S., Deng, J., Chu, H.M., Zheng, K.B., 2007. Sequence stratigraphic framework and palaeogeographical evolution of the Permian Leping series of Dian–Qian–Gui basin and its adjacent areas. Sci. China Ser. D Earth Sci. 37 (5), 605–617 (in Chinese).

Migaszewski, Z.M., Gałuszka, A., 2015. The characteristics, occurrence, and geochemical behavior of rare earth elements in the environment: a review. Crit. Rev. Environ. Sci. Technol. 45 (5), 429–471.

Mordberg, L.E., Stanley, C.J., Germann, K., 2000. Rare earth element anomalies in crandallite group minerals from the Schugorsk bauxite deposit, Timan, Russia. Eur. J. Mineral. 12 (6), 1229.

Nesbitt, H.W., 1979. Mobility and fractionation of rare earth elements during weathering of a granodiorite. Nature 279 (17), 206–210.

Nesbitt, H.W., Markovics, G., 1997. Weathering of granodioritic crust, long-term storage of elements in weathering profiles, and petrogenesis of siliciclastic sediments. Geochim. Cosmochim. Acta 61 (8), 1653–1670.

Nesbitt, H.W., Young, G., 1982. Early Proterozoic climates and plate motions inferred from major element chemistry of lutites. Nature 299 (5885), 715–717.

Nesbitt, H.W., MacRae, N.D., Kronberg, B.I., 1990. Amazon deep-sea fan muds: light REE enriched products of extreme chemical weathering. Earth Planet. Sci. Lett. 100 (1–3), 118–123.

Palacios, C.M., Hein, U.F., Dulski, P., 1986. Behaviour of rare earth elements during hydrothermal alteration at the Buena Esperanza copper–silver deposit, northern Chile. Earth Planet. Sci. Lett. 80 (3–4), 208–216.

Patino, L.C., Velbel, M.A., Price, J.R., Wade, J.A., 2003. Trace element mobility during spheroidal weathering of basalts and andesites in Hawaii and Guatemala. Chem. Geol. 202 (3–4), 343–364.

Prudencio, M.I., Braga, M.A.S., Gouveia, M.A., 1993. REE mobilization, fractionation and precipitation during weathering of basalts. Chem. Geol. 107 (3–4), 251–254.

Qiu, Y.Z., Wang, Z.G., Zhao, Z.H., 1981. The discussion of rare earth element in iron-constructures. Geochemistry 3, 220–231 (in Chinese with English abstract).

Rollinson, H.R., 1993. Using Geochemical Data: Evaluation, Presentation, Interpretation. Longman Singapore Press, pp. 1–208.

Roser, B.P., Korsch, R.J., 1988. Provenance signatures of sandstone–mudstone suites determined using discriminant function analysis of major-element data. Chem. Geol. 67 (1–2), 119–139.

Simandl, G.J., 2014. Geology and market-dependent significance of rare earth element resources. Mineral. Deposita 49 (8), 889–904.

Sverjensky, D.A., 1984. Europium redox equilibria in aqueous solution. Earth Planet. Sci. Lett. 67 (1), 70–78.

Viers, J., Dupré, B., Polvé, M., Schott, J., Dandurand, J.L., Braun, J.J., 1997. Chemical weathering in the drainage basin of a tropical watershed (Nsimi-Zoetele site, Cameroon): comparison between organic-poor and organic-rich waters. Chem. Geol. 140 (3–4), 181–206.

Walter, A.V., Nahon, D., Flicoteaux, R., Girard, J.P., Melfi, A., 1995. Behaviour of major and trace elements and fractionation of REE under tropical weathering of a typical apatite-rich carbonatite from Brazil. Earth Planet. Sci. Lett. 136 (3–4), 591–602.

Wang, W., Yang, R.D., Bao, M., Wei, H.R., Wang, Q., 2006. Study on the chemical component of the leaves of weathering Emeishan basalts in Guizhou Province. J. Guizhou Univ. Nat. Sci. 23 (4), 366–370 (in Chinese with English abstract).

Wang, Q., Deng, J., Liu, X., Zhang, Q., Sun, S., Jiang, C., Zhou, F., 2010. Discovery of the REE minerals and its geological significance in the Quyang bauxite deposit, West Guangxi, China. J. Asian Earth Sci. 39 (6), 701–712.

Wu, C.Y., Huang, D.H., Guo, Z.X., 1990. REE geochemistry in the weathered crust of granites, Longnan area, Jiangxi Province. Acta Geol. Sin. 3 (2), 193–209.

Xie, J.R., 1963. The Pandect of Deposits in China. Academic Books and Periodicals Publish, Beijing, pp. 1–6 (in Chinese).

Xu, Y.G., Chung, S.L., Jahn, B., Wu, G., 2001. Petrologic and geochemical constraints on the petrogenesis of Permian–Triassic Emeishan flood basalts in southwestern China. Lithos 58 (3–4), 145–168 (in Chinese with English abstract).

Xu, L.Z., Zhang, Z.W., Zhang, Q., Zhu, X.Q., Zhu, C.H., Huang, Y., Hang, H.M., 2006. The age of siliceous shale in the lower part of the Xuanwei Formation in Weining and its geological implication. Acta Mineral. Sin. 26 (4), 387–394 (in Chinese with English abstract).

Yang, Y.X., Zhang, N.X., 1991. The Clay Mineral of China. Geological Publishing House, Beijing, pp. 52–53 (in Chinese with English abstract).

Yang, R., Wang, W., Zhang, X., Liu, L., Wei, H., Bao, M., Wang, J., 2008. A new type of rare earth elements deposit in weathering crust of Permian basalt in western Guizhou, NW China. J. Rare Earths 26 (5), 753–759.
Yang, B.Y., Hu, B., Bao, Z.Y., Zhang, Z.G., 2011. REE geochemical characteristics and depositional environment of the blackshale-hosted Baiguoyuan Ag–V deposit in Xingshan, Hubei Province, China. J. Rare Earths 29 (5), 499–506.
Yin, H.F., 1994. Advancements of Permian and Triassic research. Adv. Earth Sci. 9 (2), 1–10 (in Chinese with English abstract).
Zhang, P.S., 1989. A study on the genetic classification of rare earth mineral deposits of China. Sci. Geol. Sin. 24 (1), 26–32 (in Chinese with English abstract).
Zhang, C.F., 1994. Properties of the weathering crust-alluvial type REE deposits in south Hunan. Hunan Geol. 13 (1), 17–21 (in Chinese with English abstract).
Zhang, Z.W., Zhu, B.Q., Chang, X.Y., Hu, Y.G., 2003. The discovery of the chalcopyrite mineralization on the formation of the Permian basalts in the western of Guizhou Province, China. Acta Mineral. Sin. 23 (2), 102 (in Chinese with English abstract).
Zhang, Z.W., Cheng, Z.D., Zhu, B.Q., 2004. The studies on the specific strata of Emeishan basalts formation are relationship with the copper mineralization. Acta Geoscienta Sin. 25 (5), 503–508 (in Chinese with English abstract).
Zhang, J., Sun, C.M., Gong, M.L., Zhang, Q., Chen, D.L., Chen, J.Y., 2007. Geochemical characteristics and occurrence states of the REE elements of the phosphorite in Xinhua, Zhijin, Guizhou. Chin. Rare Earths 28 (1), 75–79 (in Chinese with English abstract).
Zhang, Z.W., Yang, X.Y., Shuang, L., Zhang, Z.S., 2010a. Geochemical characteristics of the Xuanwei Formation in West Guizhou: significance of sedimentary environment and mineralization. Chin. J. Geochem. 29 (4), 355–364.
Zhang, Z.W., Yang, X.Y., Wen, H.J., 2010b. The enrichment of Ga within Xuanwei Formation, western Guizhou, China. Bull. Mineral. Petrol. Geochem. 29 (1), 107–108 (in Chinese).
Zhao, Z.H., Xiong, X.L., Han, L.D., 1999. Discussion on the formation mechanism of the Tetrad Effect of granite rare earth element: taking the Qianlishan and Baerzhe granite as an example. Sci. China. Ser. D Earth Sci. 29 (4), 331–338 (in Chinese with English abstract).
Zhong, H., Xu, G.W., Zhu, W.G., Hu, R.Z., He, D.F., 2009. Petrogenesis of the Taihe granite in the Emeishan Large Igneous Province and its tectonic implications. Bull. Mineral. Petrol. Geochem. 28 (2), 99–110 (in Chinese with English abstract).
Zhou, M.F., Malpas, J., Song, X.Y., Robinson, P.T., Sun, M., Kennedy, A.K., Lesher, C.M., Keays, R.R., 2002. A temporal link between the Emeishan large igneous province (SW China) and the end-Guadalupian mass extinction. Earth Planet. Sci. Lett. 196 (3–4), 113–122.
Zhou, L.J., Zhang, Z.W., You, F.H., Li, Y.J., 2013. Geological and geochemical characteristics in the paleo-weathering crust sedimentary type REE deposits, western Guizhou, China. J. Asian Earth Sci. 73, 184–198.
Zhu, B.Q., Hu, Y.G., Zhang, Z.W., Chang, X.Y., 2003. Discovery of the copper deposits with features of the Keweenawan type in the border area of Yunnan and Guizhou provinces. Sci. China Ser. D Earth Sci. 46, 60–72.